# The piRNA pathway sustains adult neurogenesis by reducing protein synthesis and cellular senescence

**Authors:**

Gasperini C.[1], Tuntevski K.[1], Pelizzoli R.[1], Lo Van A.[1], Mangoni D.[2], Cossu R.M.[2], Pascarella G.[3], Bianchini P.[4], Bielefeld P.[5], Scarpato M.[2], Pons-Espinal M.[1], Sanges R.[2, 6], Diaspro A.[4], Fitzsimons C.P.[5], Carninci P.[4,7], Gustincich S.[2] and De Pietri Tonelli D[1]*

**Affiliations:**

1) Neurobiology of miRNA Laboratory, Istituto Italiano di Tecnologia, Genoa (Italy)
2) Central RNA Laboratory, Istituto Italiano di Tecnologia, Genoa, (Italy)
3) Division of Genomic Technologies, RIKEN Center for Life Science Technologies, Yokohama (Japan)
4) Nanoscopy, CHT Erzelli, Istituto Italiano di Tecnologia, Genoa (Italy)
5) Swammerdam Institute for Life Sciences, Faculty of Science, University of Amsterdam (The Netherlands)
6) Area of Neuroscience, SISSA, Trieste (Italy)
7) Human Technopole, Milan (Italy).

* **Corresponding Author**: Davide De Pietri Tonelli; Istituto Italiano di Tecnologia (IIT); Via Morego 30, 16163 Genova (Italy); Phone +39 010 2896 725; E-mail davide.depietri@iit.it

**Keywords:**

Adult Neurogenesis; Piwi interacting RNAs; Aging; Translation

**Summary**

Adult Neural progenitor cells (aNPCs) ensure lifelong neurogenesis in the mammalian hippocampus. Proper regulation of aNPC fate entails important implications for brain plasticity and healthy aging. Piwi proteins and the small noncoding RNAs interacting with them (piRNAs) are best known in gonads as repressors of transposons. Here, we show that Piwil2 (Mili) and piRNAs are abundant in aNPCs of the postnatal mouse hippocampus and demonstrate that this pathway is essential for proper neurogenesis. Particularly, depleting the piRNA pathway in aNPCs impaired neurogenesis, increased senescence and accordingly the generation of reactive glia. Moreover, this manipulation primarily elevated 5S ribosomal RNA, SINEB1 and mRNAs encoding ribosomal proteins and regulators of translation, resulting in higher polysome density and protein synthesis upon differentiation. Our results provide evidence of an essential role for the piRNA pathway in maintaining homeostasis to sustain neural stem cell fate, underpinning its possible involvement in brain plasticity and successful aging.

## Introduction

A regulated balance of neural progenitor cells' (aNPCs) quiescence, proliferation and differentiation guarantees lifelong neurogenesis in the adult hippocampus (Altman, 1962; Doetsch et al., 1999), prevents the generation of reactive glia (Encinas et al., 2011; clarke 2018; Sierra et al., 2015), and neurodegeneration (Toda et al., 2019). Understanding the molecular control of aNPCs fate is pivotal to develop novel therapies to prevent or delay age dependent-loss of neurogenesis and related pathological conditions.

Piwi belong to an evolutionary conserved subfamily of Argonaute proteins that bind to Piwi-interacting RNAs (piRNAs), single-stranded noncoding RNAs of 21-35 nucleotides. These Piwi proteins and piRNAs (henceforth referred to as the piRNA pathway) are highly abundant in gonads, where they mainly target transposable elements (TEs) for degradation to maintain germline stem cell pools and male fertility (Czech et al., 2018; Ozata et al., 2019).

Since its initial discovery, the piRNA pathway has been implicated in regulating gene expression outside of the germline. Moreover, it is preferentially expressed in germ cells, embryonic stem cells and adult stem cells, compared to their differentiated progeny (Rojas-Ríos and Simonelig, 2018). Indeed, expression of Piwi proteins was observed in human hematopoietic stem cells, suggesting a possible role of this pathway in maintaining the stem cell pool (Sharma et al., 2001), whereas its function is dispensable for normal hematopoiesis in mouse (Nolde et al., 2013).

In the adult brain, the piRNA pathway was proposed to control synaptic plasticity and memory (Lee et al., 2011; Leighton et al., 2019; Nandi et al., 2016; Zhao et al., 2015). PiRNA levels in neurons, however, are low compared to germline cells (Lee et al., 2011; Nandi et al., 2016), disputing the proposed piRNA pathway function in the nervous system. Apart from gonads, the highest piRNA expression in adult mice has been found in the hippocampus (Perera et al., 2019), however, the specific cell type in which piRNA expression takes place was not identified. Concomitantly, transposable element (TE) expression is high in differentiating NPCs (Muotri et al., 2005), and Piwil1 (Hiwi) was recently shown to regulate human glioma stem cell maintenance (Huang et al., 2021). Thereby, it is reasonable to hypothesize that the piRNA pathway may play a role in aNPCs maintenance and/or differentiation as well.

63 Here, we demonstrate that the piRNA pathway is enriched in aNPCs, and that its function is essential for
64 proper neurogenesis. Moreover, we show that inhibiting this pathway in aNPCs leads to senescence-
65 associated inflammation in the postnatal mouse hippocampus, a condition which has been linked to age-
66 related impairment of neurogenesis and increase in astrogliogenesis (Clarke et al., 2018; Encinas et al.,
67 2011). Our results implicate the piRNA pathway in the aging of the hippocampal stem cell niche.

68 **Results**

69 **Mili expression is abundant in aNPCs and depleted in neurogenesis**

70 As an entry point to investigate Piwi pathway in aNPCs we quantified expression of *Piwil1* (Miwi) *Piwil2*
71 (Mili) and *Piwil4* (Miwi2) mRNAs, which encode the essential proteins for piRNA biogenesis and function
72 in mammals (Czech et al., 2018; Ozata et al., 2019), in cultured aNPCs derived from neural stem cells (NSC)
73 of the adult mouse Dentate Gyrus (DG) (Babu et al., 2011; Pons-Espinal et al., 2017), by RNA sequencing
74 (RNA seq) (Fig.1A). Of the three main Piwi genes in mouse, Mili was the most abundant in aNPCs, and its
75 expression increased transiently upon induction of their spontaneous differentiation. The Mili transcript was
76 particularly more abundant at day 4 (here referred to as days of differentiation DIF 4) upon onset of
77 spontaneous differentiation compared to undifferentiated (i.e., proliferating) aNPCs (DIF 0), whereas it was
78 depleted in differentiated cells (DIF 7-14) (Fig 1A). Similarly, the Mili protein abundance (Fig. 1B) was
79 higher in undifferentiated aNPCs (DIF 0) or early upon onset of vector-induced neurogenesis (DIF 4,
80 neuroblasts) than in differentiated neurons (DIF 7-14). Next, we quantified the abundance of Miwi and Mili
81 proteins in the mouse testis, whole hippocampus, and compared it to the one in undifferentiated aNPCs (Fig.
82 1C, D). As expected, the Miwi protein was very abundant in testis, but was not detectable in the whole
83 hippocampus or aNPCs (Fig.1C), whereas the Mili protein abundance in aNPCs was about 40% of the one in
84 the testes (Fig. 1D), and about four-fold higher than in primary hippocampal neurons (Fig. 1E). To validate
85 this finding *in vivo*, we used a previously published split-Cre viral approach to selectively label NSCs and
86 their progeny in the hippocampus of postnatal Td-Tomato Cre-reporter mice (Beckervordersandforth et al.,
87 2014; Pons-Espinal et al., 2017). Five days post viral-injection (dpi), we found Mili protein presence in Td-
88 Tomato positive (Td+) NSCs of the subgranular zone (SGZ) of the DG (Fig. 1F). To quantify *Mili* during
89 neurogenesis *in vivo*, we sorted Td+ NSCs and their differentiated progeny at 10 and 30 dpi in the postnatal
90 mouse hippocampus, respectively. The *Mili* transcript was significantly more abundant in Td+ NSCs (10 dpi)

91 than in adult-born Td+ neurons (30dpi) or Td- cells (Fig. 1G). These results demonstrate that Mili expression
92 is enriched in neural stem/progenitor cells and depleted in their progeny.

93 **Level of piRNAs parallels Mili abundance in neurogenesis**

94 We next wished to determine whether piRNAs are found in aNPCs and quantify their abundance in
95 neurogenesis by small RNA seq (Fig. 2). Following a previously published analysis pipeline (Ghosheh et al.,
96 2016), we identified a total of 725,472 *bona fide* piRNAs, of which 33,396 perfectly aligned (*i.e,* no
97 mismatch) with those previously annotated in the piRNA database (piRBase (Zhang et al., 2014)), had an
98 average length of 30 nt (Fig. 2A) and bore a 5' uridine (U) bias (Fig. 2B). Moreover, the distance probability
99 between the 5' termini of putative primary and secondary piRNAs was distributed similarly to that of other
100 animals (Gainetdinov et al., 2018), with asymptotic convergence around the '0' mark on the abscissa (Fig.
101 2C). Mature piRNAs typically bear 2'-*O*-methylation at their 3' termini, which confers them stability and
102 enables stronger binding to Piwi proteins (Czech et al., 2018; Ozata et al., 2019). We tested whether the
103 putative piRNAs isolated from aNPCs were also methylated by evaluating their resistance to periodate
104 oxidation and alkaline ß-elimination, as previously reported (Kirino and Mourelatos, 2007). Indeed, a
105 quantitative real time PCR (qPCR)-based small RNA assay (Taq-Man) indicated that some of the most
106 abundant piRNAs expressed in aNPCs exhibited resistance to periodate treatment, thus indicating their
107 methylation (Fig 2D). In contrast, control synthetic RNAs or endogenous small noncoding RNAs, such as
108 snoRNA bearing a terminal 2',3'-hydroxyl group, were oxidized after the treatment and therefore degraded
109 (Fig 2D). Furthermore, to assess whether putative piRNAs were depending on Mili, we quantified their
110 expression in aNPC cultures upon *Mili* knockdown (Mili-KD) achieved by transducing short-hairpin RNAs
111 targeting *Mili* transcripts, or a scramble short-hairpin RNA as control (or two different synthetic GapmeRs
112 targeting *Mili,* Fig. S1), through a viral vector-mediated protocol *in vitro*. Indeed, reduction of Mili protein
113 abundance in aNPCs (Fig.2E) was sufficient to deplete four of the most highly expressed piRNAs in aNPCs
114 (Fig. 2F and Fig. S1), in agreement with the conclusion that Mili is the most abundant Piwi protein in these
115 cells (Fig.1). Of note, this manipulation did not affect Miwi expression, excluding possible compensatory
116 effects (Fig. S1). Together, this evidence indicates that the most abundant sequences homologous to known
117 piRNAs found in aNPCs fulfill at least five of the criteria that characterize *bona fide* piRNAs (*i.e.*, length, U-
118 Bias, 2'-O-Methylation at the 3' end, inter-distance and MILI dependence).

119 Genomic mapping of the piRNA reads from aNPCs and their progeny identified 298 clusters perfectly
120 aligning to the mouse genome (Fig 2G and Table S1), with an average size of 168 bases and some of them
121 exceeding 2000 bases, as seen in mouse testes (Aravin et al., 2006; Girard et al., 2006). The piRNA raw
122 reads/cluster averaged around 4700 reads, with two clusters, one located in the chromosome 13 and one in
123 the 17, giving rise to more than 80,000 piRNA reads (Fig. 2G). Analysis of small RNA seq data for
124 directionality suggested a strand bias where the majority of the piRNAs arise unidirectionally, although
125 bidirectional piRNAs were also identified. Analysis of piRNA transcript levels in neurogenesis indicated a
126 transient peak at the onset of differentiation (Fig. 2H DIF 4 and Fig. S1), in agreement with the Mili
127 expression pattern. Next, we validated four of the most abundant piRNA clusters in Td+ NSCs sorted from
128 the adult hippocampus confirming their expression *in vivo* (Fig. 2I). Interestingly, one of the piRNA-clusters
129 in our dataset (i.e., piR-cluster 1) is homologous to the human piR-61648 that was recently shown to be
130 selectively expressed in somatic tissues, but is depleted in gonads (Torres et al., 2019) Fig. S1 and Table S1).
131 This observation prompted us to extend our analysis to human NSCs. Analysis of small RNA datasets from
132 the RIKEN FANTOM5 project (De Rie et al., 2017) confirmed the enriched expression of piR-cluster 1, as
133 well as of many additional piRNA clusters in human NSCs compared to differentiated brain cells (Fig. 2L
134 and Table S2). Together, these results indicate that piRNAs are selectively enriched in both mouse and
135 human neural stem/progenitor cells, thus matching the expression of Mili (Fig.1).

136 **The piRNA pathway sustains proper neurogenesis**

137 To infer functions of the piRNA pathway in aNPCs differentiation, we knocked down (KD) *Mili* by injecting
138 a synthetic antisense oligonucleotide (GapmeR, MILI KD), or a scrambled GapmeR (Control), in the
139 postnatal mouse hippocampus (Fig. 3A). Mili-KD (Fig. 3B) did not alter stemness or growth of aNPCs *in*
140 *vitro* (Fig. S2) but led to a dramatic increase in the expression of the glial cell marker glial fibrillary acidic
141 protein (GFAP) as early as 48 hours after GapmeR injection *in vivo* (Fig.3B) and *in vitro* (Fig. S2).
142 Inspection of brain sections 30 days after bilateral injections indicated a marked increase in GFAP+ cells
143 with enlarged somas in the ipsilateral hippocampus injected with GapmeR antisense to *Mili*, compared to
144 cells in the contralateral side injected with control GapmeR (Fig. 3C). To ascertain whether GFAP+ cells
145 were actively generated upon Mili-KD, we administered bromodeoxyuridine (BrdU) immediately after
146 GapmeRs injection to label dividing cells in a third cohort of mice (Fig. 3A). 30 days after GapmeR

injection, we found that Mili-KD led to a significant increase in adult born GFAP+BrdU+ glial cells at the expense of NeuN+BrdU+ neurons (Fig. 3D). This result was corroborated by gene set analysis in RNA seq data from differentiating aNPCs *in vitro,* showing an enrichment in the expression of astrocyte-related genes and a concomitant deregulation of neuronal fate genes upon piRNA pathway depletion (Fig S2). These results indicated that the piRNA pathway is required to sustain neurogenesis in the postnatal hippocampus at the expense of gliogenesis.

Increased GFAP expression is generally regarded as a hallmark of astrocyte reactivity (Escartin et al., 2021). In agreement, we observed a significant increase in the levels of known reactive glial markers (Clarke et al., 2018; Liddelow et al., 2017) upon Mili KD in the postnatal hippocampus (Fig. 3E). To confirm this result, we took advantage of Kainic Acid injection in the postnatal hippocampus of mice expressing GFP under the control of the NSCs/NPCs specific promoter *Nestin* (Fig. 3F), a treatment previously shown to induce aNSC conversion into reactive glia (Bielefeld et al., 2017; Sierra et al., 2015). Indeed, this treatment reduced levels of the piRNA pathway in sorted *Nestin*-GFP+ NSCs (Fig. 3F). Altogether, these results demonstrate an essential role of the piRNA pathway for proper neurogenesis and suggest that its downregulation mediates reactive gliogenesis in the postnatal mouse hippocampus.

**Inhibition of the piRNA pathway in aNPCs results in senescence-associated phenotypes**

Conversion of hippocampal NSC into reactive glia, at the expense of neurogenesis, has been observed in normal aging (Clarke et al., 2018), and it has been related to increased neuroinflammation and cellular senescence (Babcock et al., 2021; Martín-Suárez et al., 2019). Whether the piRNA pathway is involved in this mechanism in the brain, is unknown. This prompted us to analyze RNA seq data for senescence-associated secretory phenotype (SASP) in Mili-KD in neuroblasts (Fig. 4A). Interestingly, we found that depletion of the piRNA pathway led to a significant increase in the expression of several immune-modulatory and senescence associated genes in neuroblasts compared to control cells (Fig. 4A). Moreover, after piRNA pathway depletion we observed a higher proportion of cells positive for senescence-associated β-galactosidase (β-gal) as early as 48 hours upon induction of their spontaneous differentiation (Fig. 4B). At the same time point, we immuno-stained aNPCs with anti-KI67 (a protein that is expressed in all phases of the cell cycle except G0 and early G1 (Yu, 1992)) and anti-BrdU antibodies. Quantification of the BrdU + and KI67- cells over total BrdU+ indicated a premature cycle exit upon piRNA pathway depletion (Fig. 4C).

175 Similarly, by propidium iodide incorporation and flow cytometry analysis we found an increase in the
176 proportion of cells in G0/G1 phase and a concomitant decrease in S phase cells (Fig. 4D). Accordingly,
177 piRNA pathway depletion did not lead to apoptosis (Fig. S3), whereas we found that it led to altered
178 expression of genes previously associated with senescence-induced cell cycle exit (Fig. 4E, F), circadian
179 mechanism and oxidative stress (Fig. S3), as previously reported (Adusumilli et al., 2021; Babcock et al.,
180 2021; Schouten et al., 2020). To corroborate this evidence *in vivo*, we quantified the expression of *Mili*
181 transcript in sorted *Nestin*-GFP+ NSCs from the DG of young (6 Weeks) and ~12 Months old mice (i.e.,
182 when the majority of hippocampal aNSCs turn into an aged phenotype (Martín-Suárez et al., 2019)) and
183 found that *Mili* transcript was reduced in aged aNSCs (Fig. 4G). These results suggest that the piRNA
184 pathway prevents aNPCs/neuroblasts senescence.

185 **The piRNA pathway modulates noncoding RNAs and mRNAs involved in ribosome assembly and**
186 **translation.**

187 Next, we sought to identify piRNA pathway targets in aNPCs lineages (Fig.5). In contrast to germline
188 piRNAs which primarily target TEs, somatic piRNAs have also homology with, or pair by sequence
189 complementarity to noncoding RNAs, such as transfer RNAs (tRNAs) (Keam et al., 2014) and others (Rojas-
190 Ríos and Simonelig, 2018). We searched for noncoding RNAs that are putative targets of the piRNAs
191 expressed in our model (Fig. 2). Indeed, TEs were just a minor percentage of the predicted noncoding RNA
192 targets in both undifferentiated aNPCs and progeny (Fig.5 A, B), despite their proportion being increased
193 upon induction of neurogenesis (Fig. 5 B). The latter finding is in agreement with the observed activation of
194 TEs (*i.e.,* LINE1) during neuronal differentiation (Coufal et al., 2009; Muotri et al., 2005). Interestingly, 5S
195 ribosomal RNA (5S rRNA) and tRNAs were the main predicted piRNA targets in both undifferentiated
196 (47% and 40%, respectively) and progeny (35% and 16%, respectively, Fig. 5 A, B). To ascertain whether
197 these noncoding RNAs are modulated by the piRNA pathway, we quantified their expression in aNPCs and
198 progeny, upon Mili-KD (Fig. 5 C, D). Indeed, piRNA pathway depletion significantly elevated levels of 5S
199 rRNA and SINE-B1 family of TEs in both undifferentiated aNPCs and progeny, compared to scrambled
200 control (Fig.5 C), whereas LINE1, here quantified with a qPCR assay detecting the full-length transcript,
201 was initially refractory to piRNA depletion and its level only increased late in differentiation (Fig. 5 D).
202 These results indicate that 5s rRNAs and SINE-B1 are repressed by the piRNA pathway in neurogenesis. To

203 identify which mRNAs are modulated by the piRNA pathway in neurogenesis, we analyzed mRNA
204 transcriptome by RNA seq from Mili KD or scrambled control cells during their spontaneous differentiation
205 at DIF 4, *i.e.,* when the piRNAs are most abundant (Fig. 2). Most of the modulated genes upon piRNA
206 pathway depletion were upregulated (Fig 5 E), and the majority of them bore sequences antisense to a
207 piRNA (*i.e.,* were predicted piRNA targets), or harbored homologous sequences to piRNAs (Fig. 5 F). We
208 found that mRNA transcripts from individual genes are targeted by multiple piRNAs, with a maximum of
209 11,904 unique piRNA sequences targeting a modulated gene (Fig. 5G). Spearman analysis indicated a
210 positive correlation between piRNA levels in undifferentiated and differentiating aNPCs/neuroblasts, and the
211 degree of target upregulation upon piRNA pathway depletion (Fig. 5H). Gene ontology (GO) analysis of the
212 upregulated piRNA targets in Mili KD cells at DIF 4 indicated a prevalence of "mRNA processing" and
213 "Translation" among the top ten biological processes affected (Fig. 5 I). Moreover "Ribosome" (p-value 7,7
214 E-8) and "Splieceosome" (p-value 3,3 E-7) were the top enriched pathways based on function in the Kyoto
215 Encyclopedia of Genes and Genomes (KEGG) database (*not shown*). This evidence is consistent with our
216 observation that 5S rRNA, SINEB1 and possibly tRNAs are modulated by the piRNA pathway in these cells.

217 **Inhibition of the piRNA pathway in aNPCs enhances polysome assembly and results in higher protein**
218 **synthesis upon differentiation.**

219 As dysregulation of ribosome biogenesis and translation have been associated to cellular senescence (Liu and
220 Sabatini, 2020), we analyzed polyribosomes in aNPCs and in their progeny. To this end we first used
221 stimulated emission depletion (STED) nanoscopy, a method that allows to visualize and quantify polysome
222 density (Viero et al., 2015). Depletion of the piRNA pathway increased polyribosomes in both
223 undifferentiated and differentiating aNPCs, as revealed by immunostaining for the ribosomal protein RPL26,
224 compared to control cells (Fig. 6A, B). As the density of ribosomes over transcript does not necessarily
225 correlate with its translation (Mills and Green, 2017), we also quantified protein synthesis rate by OPP (O-
226 propargyl-puromycin) labelling of nascent proteins during neurogenesis. Accordingly, protein synthesis rate
227 was significantly increased upon piRNA pathway depletion in differentiating cells, but not in
228 undifferentiated aNPCs (Fig. 6C, DIF 7).

229 In sum, these results support a role for the piRNA pathway in sustaining adult neurogenesis by repressing
230 translation and senescence in aNPCs.

231 **Discussion**

232 In this study, we investigated the expression of Mili and Mili-dependent piRNAs in mouse and human NPCs,
233 and inferred functions of this pathway in the regulation of neurogenesis in the adult mouse hippocampus.
234 Our results provide evidence of an essential role for the piRNA pathway in mammalian neurogenesis. This
235 finding adds a new layer of complexity to the understanding of adult brain plasticity and aging, and entails
236 crucial implications for neuronal disorders where dysregulated expression of the piRNA pathway has been
237 reported, such as neurodegeneration (Jain et al., 2019; Wakisaka, 2019).
238 Differently to the canonical functions of the piRNA pathway in germline, which are mainly required for
239 maintenance of stem cell pools, here we provide the first evidence of a requisite role linking the piRNA
240 pathway with proper differentiation and fate choice of neural stem cells. Specifically, we show that piRNA
241 pathway inhibition in aNPCs leads to aberrant neurogenesis, and to an increased generation of reactive
242 astrocytes, a phenotype which has been observed in the hippocampi of aged mice (Bonaguidi et al., 2011;
243 Clarke et al., 2018; Encinas et al., 2011; Martín‐Suárez et al., 2019). Accordingly, we find that inhibition of
244 piRNA biogenesis in aNPCs results in senescence-like phenotype, thus providing a possible cellular
245 mechanism that drives aNPC fate adrift toward reactive astrocytes.
246 Moreover, and in agreement with previous observations linking cell senescence to altered ribosome
247 biogenesis (Liu and Sabatini, 2020), our data suggest pleiotropic functions of the Mili and Mili-dependent
248 piRNAs in aNPCs reduce polysome assembly and protein synthesis. This result differs from previous
249 functional evidence for the piRNA pathway in germline stem cells, where Miwi/Maelstrom interacting
250 piRNAs activate translation to sustain spermiogenesis (Castañeda et al., 2014; Dai et al., 2019).
251 Despite the precise cascade of events that lead to dysregulation of NSCs homeostasis in aging is only
252 beginning to emerge, proper control of proteostasis, pro-neurogenic, cell cycle and pro-inflammatory
253 signaling is involved in maintenance of lifelong neurogenesis. Our study about Mili and its targets in mouse
254 NSCs certainly provides an entry point to dissect the role of the piRNA pathway in mammalian neurogenesis
255 in the context of brain aging.

256 **Methods**

257 **Lead contact and materials availability:**

258 Further information and requests for resources and reagents should be directed to and will be fulfilled by the
259 Lead Contact, Davide De Pietri Tonelli (davide.depietri@iit.it).

260 **Materials and Methods**

261 **Mice**

262 C57BL/6 and Td-Tomato$^{flox/wt}$ knock-in reporter mice (Jackson Laboratory stock number 007908) (Madisen
263 et al., 2010), were housed at *Istituto Italiano di Tecnologia* (IIT); Nestin-GFP mice (Mignone et al., 2004) for
264 the Kainic Acid experiments were housed at the Swammerdam Institute for Life Sciences, University of
265 Amsterdam. All animal procedures were approved by IIT animal use committee and the Italian Ministry of
266 health, or by the Commission for Animal Welfare at University of Amsterdam (DEC protocol 4925,
267 AVD1110020184925), respectively and conducted in accordance with the Guide for the Care and Use of
268 Laboratory Animals of the European Community Council Directives. All mice were group-housed under a 12-
269 h light-dark cycle in a temperature and humidity-controlled environment with ad libitum access to food and
270 water.

271 **aNPCs cultures**

272 Hippocampal NPCs were prepared and expanded as described previously (Babu et al., 2011; Pons-Espinal et
273 al., 2019; Walker and Kempermann, 2014) and induction of spontaneous differentiation by growth factor
274 removal was done as previously described (Pons-Espinal 2017, and Pons-Espinal, Gasperini et al 2019); viral
275 induced-neuronal differentiation of aNPCs was done by transduction of a viral construct expressing Ascl1-
276 ERT2 as previously described (Braun et al., 2013).

277 **Protein extraction and Western blot**

278 For total protein extraction, adult testes or hippocampus or cell pellets were homogenized in RIPA buffer and
279 the protein concentration was determined using a Bradford Assay kit (Bio-Rad). For blot analysis, equal
280 amounts of protein (30 µg) were run on homemade 10% polyacrylamide gels and transferred on nitrocellulose
281 membranes (GE Healthcare). Membranes were probed with primary antibodies (listed in the table below),
282 followed by HRP-conjugated secondary antibody anti-rabbit or mouse (Invitrogen, A16104, A16072; 1:2,000).

283 The band corresponding to Mili protein was detected with two different antibodies and validated with four
284 different RNAi constructs (1 shRNA virus and 3 GapmeRs). LAS 4000 Mini Imaging System (GE Healthcare)
285 was used to digitally acquire chemiluminescence signals, and the band intensities were quantified using Fiji
286 (Macbiophotonics, Fiji is Just ImageJ) (Schindelin et al., 2012). List of antibodies used available in the SI
287 appendix.

288 **Virus and GapmeR injection**

289 Virus or GapmeR injection was done as previously shown (Pons-Espinal et al., 2019): 8 weeks-old mice Td-
290 Tomato$^{flox/wt}$ or WT C57BL6/J were anesthetized with isoflurane, 1 µl of virus mix (Split-Cre N-Cre:C-Cre)
291 or 1.5 µl of antisense LNA GapmeR for Mili-KD or negative control (MILI 339511, Control 339515, Qiagen),
292 were stereotaxically injected in the dentate gyrus. To assess the efficacy of *Mili* knockdown, a first group of
293 mice (n=5) was sacrificed 48 hours after the injection and the DG dissected for RNA or protein extraction. 24
294 hours after the oligos injection another set of animals received 2 BrdU intraperitoneal injections per day for 5
295 days (50 mg/kg) (one every 12 hours). Animals were sacrificed 10 (n=5) or 30 days after oligos injection (n=7)
296 for histological analysis, as previously described (Pons-Espinal et al., 2019). Mice were anesthetized with
297 intraperitoneal administration of ketamine (90mg/kg) and xylazine (5-7mg/kg), and subsequently perfused
298 with PBS followed by 4% paraformaldehyde (PFA). Brains were harvested, postfixed overnight in 4% PFA,
299 and then equilibrated in 30% sucrose. 40 µm brain sections were generated using a sliding microtome and were
300 stored in a −20°C freezer as floating sections in 48 well plates filled with cryoprotectant solution (glycerol,
301 ethylene glycol, and 0.2 M phosphate buffer, pH 7.4, 1:1:2 by volume). Slices were used for
302 immunofluorescence and immunohistochemical analysis.

303 **Fluorescence-Activated Cell Sorting (FACS) and flow cytofluorometric analysis of cell cycle**
304 **distribution**

305 For RNA extraction and cDNA preparation, Td-Tomato$^{flox/wt}$ or Nestin-GFP mice were used. Six to ten Td-
306 Tomato$^{flox/wt}$ mice were euthanized 10 or 30 days after the split cre viruses injection. DG cells were
307 dissociated with the Neural Tissue Dissociation Kit P (Miltenyi Biotec) and FACS-sorted as previously
308 published (Walker et al., 2016). FACS-sorted cells were immediately processed for RNA extraction. To
309 measure the cell cycle length, we used propidium iodide (PI), which binds to DNA by intercalating between
310 the bases, as previously described (Krishan). Briefly, cells were trypsinized, resuspended in PBS and fixed

311 with 70% of ethanol for 40 minutes on ice. Cells were then centrifuged, resuspended in PBS for 15 minutes
312 and then incubated 1h at 37°C with 60 µg/ml of PI (Sigma). Cells were collected by centrifuge and
313 resuspended in ice-cold PBS for FACS analysis.

314 **Immunostaining analysis**

315 The immunostaining on brain slices was performed on sections covering the entire dorsal hippocampus as
316 previously described (Paxinos, 2001; Pons-Espinal et al., 2019). To detect Ki67 staining, citrate buffer 10 mM
317 pH = 6 treatment during 10 min at 95 °C was used. Primary antibodies are listed below, secondary fluorescent
318 antibodies were diluted 1:1000 (Goat Alexa 488, 568, and 647nm, Invitrogen). Confocal stack images of brain
319 slices (40µm) were obtained with the Confocal A1 Nikon Inverted SFC with 20x objective. Cell quantification
320 and analysis was performed using NIS-Elements software (Nikon) and the Cell-counter plugin in Fiji.
321 Immunofluorescence staining on cell cultures was performed as reported in (Pons-Espinal et al., 2019). To
322 detect BrdU incorporation, cells were pretreated with 2N HCl for 30 min at 37°C. Cells were mounted in
323 mounting medium and counterstained with fluorescent nuclear dye DAPI (Invitrogen). Images were obtained
324 using the microscope Nikon Eclipse at 20x or 40x magnification and quantification was performed using a
325 Cell-counter plugin in Fiji. DAB staining was performed as previously reported (Bielefeld et al., 2019). Briefly,
326 sections were incubated with peroxidase block (Vectashield), permeabilized with 0.3% PBS-Triton X (PBS-
327 T) and 0.1% PBS-T. Sections were blocked with 0.1% PBS-T and 5% Normal Goat Serum (NGS), incubated
328 with primary antibodies and subsequently with the corresponding biotinylated secondary antibodies (1:1000
329 Goat anti-rabbit, Invitrogen). Signal amplification was performed using the ABC complex (Vectashield),
330 according to manufacturer's instructions. Sections were incubated with the solution for DAB reaction (Sigma)
331 and counterstained with Hoechst (1:300), mounted and cover slipped with Vectashield reagent (VECTOR
332 Labs). List of antibodies used available in the SI Appendix.

333 **RNA extraction and real time qPCR**

334 Total RNA was extracted from aNPCs (proliferating and differentiating conditions), or DG dissected from
335 adult C57BL/6, Nestin-GFP or Td-Tomato$^{flox/wt}$ mice with QIAzol protocol (Qiagen) according to the
336 manufacturer's instructions. 1 µg of total RNA was treated with DNase I (Sigma) and cDNA was synthesized
337 using iScript cDNA Synthesis kit (Bio-Rad) or with ImProm-II reverse transcriptase (Promega). Real time
338 qPCR was performed in duplex with Actin or Ubiquitin C as a reference gene, with QuantiFast SYBR Green

339 PCR Kit (Qiagen) or Taqman Assay (Thermo Fisher) on ABI-7500 Real-Time PCR System (Applied
340 Biosystems). Expression levels were determined relative to Ubiquitin C or Actin, using delta delta Ct method.
341 Primers listed below were designed using NCBI/UCSC Genome Browser and Primer3 software tools and then
342 checked in PrimerBLAST for their specificity to amplify the desired genes. List of primers used available in
343 the SI Appendix.

344 **Small RNA library preparation**

345 Cells were lysed in QIAzol lysis reagent and total RNA was isolated using the miRNeasy Mini kit (Qiagen),
346 according to the manufacturer's instructions. Quantity and quality of the total RNA were measured by
347 Nanodrop spectrophotometer and Experion RNA chips (Bio-Rad). RNA with RNA integrity number (RIN)
348 values ≥ 9.5 were selected for the study. 1 μg of high-quality RNA for each sample was used for library
349 preparation according to the Illumina TruSeq small RNA library protocol (Illumina Inc., CA). Briefly, 3'
350 adapters were ligated to 3' end of small RNAs using a truncated RNA ligase enzyme followed by 5' adaptor
351 ligation using RNA ligase enzyme. Reverse transcription followed by PCR was used to prepare cDNA using
352 primers specific for the 3' and 5' adapters. The amplification of those fragments having adapter molecules on
353 both ends was carried out with 13 PCR cycles. The amplified libraries were pooled together and run on a 6%
354 polyacrylamide gel. The 145-160 bp bands (which correspond to inserts of 24-32 nt cDNAs) were extracted
355 and purified using the Wizard® SV Gel and PCR Clean-Up System (Promega). The quality of the library was
356 assessed by the Experion DNA 1K chips (Bio-Rad). Small RNA sequencing using HiSeq2000 (Illumina Inc.,
357 CA) was performed by the Center for Genomic Science of IIT@SEMM.

358 **Mili knock down *in vitro***

359 To constitutively knockdown Mili expression *in vitro*, aNPCs were infected at MOI=5 with a lentivirus
360 encoding for a *Mili*-targeted short hairpin (shMILI, plKO.1, Sigma), or for a short hairpin scramble lentivirus
361 (Control, SHC202, Sigma) both decorated with an eGFP reporter. GFP-positive cells were first selected by
362 FACS after three passages, and then plated in proliferating or differentiating media, as previously described.
363 We also performed the knock down using two different synthetic antisense LNA GapmeRs for Mili-KD or
364 negative control (Mili 339511, Control 339515, Qiagen). Mili knock down was assessed by real time qPCR
365 and Western Blot.

366 **mRNA library preparation**

aNPCs WT and transduced with the Control or with the shMILI lentiviruses, were grown to confluence and allowed to spontaneously differentiate for the indicated days. Total RNA was extracted using QIAzol lysis reagent and quantity and quality of the total RNA were measured by Qubit 4 Fluorometer (Thermo Fisher) and Bioanalyzer RNA chips (Agilent). RNA with RNA integrity number (RIN) values ≥ 8 were selected for the study. 30 ng of high-quality RNA for each sample was used for library preparation according to the Illumina Stranded Total RNA Prep, Ligation with Ribo-Zero Plus Kit (20040529, Illumina Inc., CA) using the IDT for Illumina Indexes Set A (20040553). Briefly, after ribosomal RNA depletion, RNA was fragmented and denatured and cDNA synthesized. Then the 3' ends were adenylated, and anchors ligated. After amplification and clean up, quality of the libraries was assessed by the Bioanalyzer DNA chips (Agilent). Paired-End stranded total RNA sequencing on NovaSeq 6000 Sequencing System instrument (Illumina Inc., CA), was performed by the IIT Genomic Unit @Center for Human Technologies.

**Small RNA sequencing data processing**

Illumina reads were trimmed to remove the 3′ adapter using Cutadapt, with parameters -m 25 -q 20. Since piRNA size ranges from 26 to 31 bases, all sequences with length ≤24 bases were discarded.

Reads mapped to known non-coding RNAs (RNAcentral v6.0 snoRNA, UCSC tRNA, miRBase Release 21 miRNA hairpin and mature miRNA annotation, NCBI complete ribosomal DNA unit) (Karolchik, 2004; Kozomara and Griffiths-Jones, 2014; Petrov et al., 2015) were removed from the datasets. The comparison was performed using NCBI BLASTN v2.6.0 with parameters -max_hsps= 1, -max_target_seqs= 1, -perc_identity= 80, mismatches <= 1, qcovhsp >= 90 (Altschul et al., 1990). Reads were aligned on the non-repeat-masked UCSC release 9 of the mouse genome (MM9) (Waterston et al., 2002) using bowtie2 (Langmead and Salzberg, 2012) v2.2.6 with the sensitive preset option and allowed a maximum of 100 alignments. All the reads that aligned to the genome were retained and used for subsequent analysis. piRNA clusters were identified collapsing overlapped piRNA sequences (piRBase Release 1) (Zhang et al., 2014) into one cluster (mergeBed with preset options) (Quinlan and Hall, 2010). piRNA clusters and all the reads that aligned to the genome were intersected (intersectBed with option -f 1). Intersection files were then parsed using a custom perl script in order to evaluate alignment counts. Differential expression was assessed using DESeq2 (Love et al., 2014). piRNA clusters were considered differentially expressed when the adjusted p-value was ≤ 0.05, and down- and up-regulation was established in the range of ≤ -1 to ≥ 1 log2 fold-change,

395 respectively. piRNA sequences were then categorized for the putative mRNA transcript targets (for each gene).
396 In order to obtain a count of piRNA target levels which target individual gene transcripts, for each
397 differentiation time-point (DIF0-7), piRNA transcripts were expressed in transcripts per million (TPM), and
398 summed for each target category. Spearman correlation was performed between the levels of the piRNA in the
399 Sh-Scramble (control) genotype, and compared to the fold-change level of the putative target genes which
400 were found to be significantly altered (up and down) in the Sh-Mili-KD genotype. In order to assess the
401 clustering behavior of putative piRNAs, the 5' termini positions of each cluster-associated putative primary
402 and putative secondary piRNA sequences were analyzed for distance, represented as probability within a range
403 of 200 nucleotides in the 5' direction and 200 nucleotides in the 3' direction of the putative primary piRNAs,
404 as reported previously (Gainetdinov et al., 2018). The positional distance between piRNAs for each cluster
405 was sampled iteratively and normalized by the total number of diverse piRNAs associated with each cluster.
406 The distance probability distribution was assayed by the locally weighted smoothing linear regression method
407 (LOWESS), by using the built-in MATLAB 'fit' function (MathWorks, Natick, MA), with a span value of 0.1.

408 **mRNA Sequencing data processing**

409 Illumina sequencing was performed bidirectionally, and in duplicate by two flowcell pairs of 100 and 150 base
410 pairs, for a total of 6 measurements produced from 3 independent samples for each differentiation time-point
411 and genotype. Adapter sequences were trimmed using *Cutadapt*, after which a quality control trim was
412 implemented on a sliding window of 25 nucleotides, for 2 base pairs with a minimum quality score of 26, with
413 the *Bowtie* build for the MATLAB bioinformatics suite (MathWorks, Natick, MA). Transcript quantification
414 was performed with the *Salmon* suite, as reported previously (Patro et al., 2017), on the NCBI mouse genome,
415 release 67, obtained from the ENSEMBL FASTA directory. The identified ENSEMBL gene accessions were
416 grouped for the different transcript reads, and the read counts, expressed in TPM, were summed for the
417 annotated transcripts. Outlier reads for each gene transcript level in TPM were detected by the mean absolute
418 deviations method (MAD), where reads with more than 3 scaled MAD distances from the mean were
419 eliminated from statistical analysis. Then, the mean and SD for each gene were used for statistical analysis
420 among the different genotypes by one-way ANOVA with multiple comparison. *P*-values lower than, or equal
421 to, 0.05 were selected as the threshold of significance, for a minimum count of 4 of 6 samples per gene.
422 Database for Annotation, Visualization and Integrated Discovery (DAVID, https://david.ncifcrf.gov/), (Huang

423 et al., 2009), was used to perform Gene ontology (GO) and Kyoto Encyclopedia of Genes and Genomes
424 (KEGG) signaling pathway analysis.

425 **Periodate oxidation and alkaline ß-elimination**

426 Periodate oxidation and alkaline ß-elimination was performed as previously described (Balaratnam et al.,
427 2018). Briefly, total small RNAs were isolated using miRneasy Mini kit (Qiagen) according to the
428 manufacture's protocol. Each sample was split in two portions, each containing 25µg of RNA and
429 independently treated with either 200 mM of sodium periodate or water, and RNA precipitated by ethanol. As
430 internal control for the assay, a synthetic piRNA sequence (corresponding to one of the most abundant piRNA
431 found in aNPCs – piR-cluster-1) either modified with the 3'-end 2'-O-methylation (positive control) or bearing
432 a terminal 2',3'-hydroxyl group (negative control) were subject to the periodate treatment as above. The
433 samples and control oligos were finally quantified by qPCR-TaqMan small RNA assay.

434 **piRNAs real time qPCR**

435 Total RNA enriched in the fraction of small RNAs, was extracted using miRNeasy Mini kit following the
436 manufacturer's instructions from aNPCs, DG extracted from C57BL6/J or Td-Tomato$^{flox/wt}$ mice. cDNA was
437 obtained using the TaqMan MicroRNA Reverse Transcription Kit (Thermo Fisher) according to the
438 manufacturer's instructions and quantified using the Custom TaqMan Small RNA Assay (Thermo Fisher) on
439 a ABI-7500 Real-Time PCR System (Applied Biosystems). Each sample was normalized to U6 snRNA level
440 (Thermo Fisher). Cluster sequences used for probe design are listed in Table S1.

441 **ß-galactosidase detection**

442 Was obtained with the Senescence Cells Histochemical Staining Kit (Sigma-Aldrich, CS0030), according the
443 manufacturer's instructions. Briefly, cells were plated on coverslip in proliferating medium. 48h after the
444 induction of spontaneous differentiation, cells were washed twice with PBS 1X and incubated with Fixation
445 Buffer 1X for 7 min at RT. Next, cells were rinsed with PBS 1X and incubated with fresh senescence-
446 associated ß-Gal (SA-ß-Gal) stain solution at 37°C (no $CO_2$) for 4 h. Reaction was blocked with PBS 1X and
447 coverslips were mounted on slides using Vectashield reagent (VECTOR Labs). Images were obtained using
448 the microscope Nikon Eclipse, the percentage of cells expressing ß-galactosidase was quantified over the
449 number of total cells using a Cell-counter plugin in Fiji software.

450 ***in silico* piRNA targets prediction**

451 For piRNA targets analysis, we divided the sequencing data in one set of 100 piRNA clusters enriched in
452 proliferating aNPCs (DIF0) and a second set of 198 clusters specifically expressed at DIF4/7 stage.
453 The Differential Expression analysis for piRNAs mapping on REs showing trends for enrichment of piRNAs
454 mapping on repeat elements (REs) in DIF4 and DIF7 compared to DIF0 was done using EdgeR software
455 package (Robinson and Oshlack, 2010). Identification of piRNA targets was divided in: piRNAs mapping on
456 REs only / piRNAs mapping on GENCODE elements / piRNAs mapping on REs within GENCODE
457 elements / unannotated piRNAs / piRNAs clusters. Gene Ontology analysis for piRNAs mapping on
458 GENCODE protein-coding genes (but NOT mapping on REs) has been done with the R package GOFuncR
459 (https://bioconductor.org/packages/release/bioc/html/GOfuncR.html)

460 **Protein synthesis assay**

461 To quantify the protein synthesis rate of cells, we used the Global Protein Synthesis Assay Kit
462 (FACS/Microscopy), Red Fluorescence kit (abcam), following the manufacturer's instructions. Briefly, cells
463 in proliferating or differentiating media (DIF7) were treated with Cycloheximide as an inhibitor of protein
464 synthesis, for 30 min at 37°C. Media were replaced with fresh aliquots containing Protein Label (400X)
465 diluted to 1X final concentration and the cells were incubated for additional 30 min at 37°C. Negative
466 control cells were not incubated with the protein label. Samples were analyzed by FACS for red fluorescence
467 generated by *de novo* synthesized protein during click reaction. Translation rate is directly proportional to
468 emitted fluorescence. Cells emitting fluorescence lower than $10^3$ were considered negative (P3), higher than
469 $10^4$ were considered positive (P2).

470 **Kainic Acid Administration, single cell suspension and enrichment of aNPCs by FACS**

471 Kainic Acid to elicit tonic, non-convulsive epileptic seizures, was administered as described before (Bielefeld
472 et al., 2019). Briefly, 50nL of 2.22mM Kainic Acid dissolved in PBS (pH 7.4) was injected bilaterally into the
473 hippocampus at the following coordinates (AP -2.0, ML +/- 1.5, DV -2.0 mm) (between 9AM and 1PM).
474 Control animals were administered saline (pH 7.4). Bilateral dentate gyri from 3 animals per condition were
475 pooled to allow sufficient recovery of NPCs. A single cell suspension was created using a Neural Tissue
476 Dissociation kit (Miltenyi Biotec), according to the manufacturers protocol. In order to enrich aNPCs from the
477 DG, we used the endogenous GFP expression driven by the Nestin promotor in combination with FACS.

478 Propium Iodide (5µg/mL) was added to the single cell suspension to assess cell viability. Cells were sorted
479 using a FACSAriatm III system (BD) with 488nm excitation laser. Cell duplets were removed based on
480 forward and side scatter and viable cells were selected based on PI negativity. GFP-positive (corrected for
481 autofluorescence) cells were sorted (≅ 50000 cells/pool) and collected in PBS containing 1% FBS. Trizol LS
482 (Thermo Scientific) was added and after resuspension samples were snap-frozen and stored at -20°C.

483 **Immunofluorescence, STED nanoscopy and particle analysis**

484 Confocal and Stimulated Emission Depletion (STED) nanoscopy were performed as previously reported
485 (Diaspro and Bianchini, 2020; Vicidomini et al., 2018). aNPCs were plated on glass coverslips 24 h before
486 fixation. Cells were fixed with PFA 4%, permeabilized with PBS-T 0.1%, blocked 1 hour at room temperature
487 with PBS-T 0.1% NGS 5% and incubated according to the dilution suggested by the manufacturer's
488 instructions with 0.01 µg/ml rabbit polyclonal antibody against the N terminus of RPL26 (Abcam) for 1 h at
489 room temperature. Cells were washed extensively and incubated with the secondary antibody goat anti–rabbit
490 ATTO-647N (0.8 µg/ml; Sigma) for 45 min. Nuclei were stained while mounting the coverslip with DAPI-
491 Prolong antifade (Invitrogen). Confocal and STED images were acquired at 23°C with a modified TCS SP5
492 STED-CW gated (Leica Microsystems, Mannheim, Germany) operated with Leica's microscope imaging
493 software. The microscope has been customized with a second pulsed STED laser line at 775nm. The beam
494 originates from a Onefive Katana HP 8 (NKT, Birkerød, Denmark) and pass through a vortex phase plate (RPC
495 photonics, Rochester, NY, USA) before entering the microscope through the IR port. The depletion laser pulses
496 are electronically synchronized with the Leica's supercontinuum pulsed and visible excitation laser. The
497 ATTO- 647N fluorescence was excited at 633 nm, and the fluorescence depletion was performed 775 nm. The
498 maximal focal power of the STED beam was 200 mW at 80 MHz. Both beams were focused into the 1.4 NA
499 objective lens (HCX PL APO 100× 1.40 NA Oil STED Orange; Leica). Fluorescence was collected by the
500 same lens, filtered with a 775 nm notch filter, and imaged in the spectral range 660–710 nm by hybrid detector
501 with a time gating of 1 ns. All of the images have 14-nm pixel size and 37-µs pixel dwell time.
502 We performed the analysis of polysome clusters in aNPCs on more than 20 images likewise different cells.
503 Image analysis was performed using the Fiji software.

504 **Quantification and Statistical analysis**

Data are presented as mean ± SEM and were analyzed using Prism 6 (GraphPad). Statistical significance was assessed with a two-tailed unpaired t test for two experimental groups. For experiments with three or more groups, one-way ANOVA with Bonferroni's multiple comparison test as post hoc was used. Results were considered significant when $p < 0.05$.

**Data and code availability**

RNA sequencing data (mouse) have been deposited in the European Nucleotide Archive (ENA) at EMBL-EBI and available upon request; human datasets are available through RIKEN FANTOM5.

513 **References**

514 Adusumilli, V.S., Walker, T.L., Overall, R.W., Klatt, G.M., Zeidan, S.A., Zocher, S., Kirova, D.G., Ntitsias,
515 K., Fischer, T.J., Sykes, A.M., et al. (2021). ROS Dynamics Delineate Functional States of Hippocampal
516 Neural Stem Cells and Link to Their Activity-Dependent Exit from Quiescence. Cell Stem Cell *28*, 300-
517 314.e6.
518 Altman, J. (1962). Are new neurons formed in the brains of adult mammals? Science (80-. ). *135*, 1127–
519 1128.
520 Altschul, S.F., Gish, W., Miller, W., Myers, E.W., and Lipman, D.J. (1990). Basic local alignment search
521 tool. J. Mol. Biol. *215*, 403–410.
522 Aravin, A., Gaidatzis, D., Pfeffer, S., Lagos-Quintana, M., Landgraf, P., Iovino, N., Morris, P., Brownstein,
523 M.J., Kuramochi-Miyagawa, S., Nakano, T., et al. (2006). A novel class of small RNAs bind to MILI protein
524 in mouse testes. Nature *442*, 203–207.
525 Babcock, K.R., Page, J.S., Fallon, J.R., and Webb, A.E. (2021). Adult hippocampal neurogenesis in aging
526 and Alzheimer's disease. Stem Cell Reports.
527 Babu, H., Claasen, J.H., Kannan, S., Rünker, A.E., Palmer, T., and Kempermann, G. (2011). A protocol for
528 isolation and enriched monolayer cultivation of neural precursor cells from mouse dentate gyrus. Front.
529 Neurosci. *5*, 89.
530 Balaratnam, S., West, N., and Basu, S. (2018). A piRNA utilizes HILI and HIWI2 mediated pathway to
531 down-regulate ferritin heavy chain 1 mRNA in human somatic cells. Nucleic Acids Res. *46*, 10635–10648.
532 Beckervordersandforth, R., Deshpande, A., Schäffner, I., Huttner, H.B., Lepier, A., Lie, D.C., and Götz, M.
533 (2014). In vivo targeting of adult neural stem cells in the dentate gyrus by a Split-Cre Approach. Stem Cell
534 Reports *2*, 153–162.
535 Bielefeld, P., Sierra, A., Encinas, J.M., Maletic-Savatic, M., Anderson, A., and Fitzsimons, C.P. (2017). A
536 Standardized Protocol for Stereotaxic Intrahippocampal Administration of Kainic Acid Combined with
537 Electroencephalographic Seizure Monitoring in Mice. Front. Neurosci. *11*.
538 Bielefeld, P., Schouten, M., Meijer, G.M., Breuk, M.J., Geijtenbeek, K., Karayel, S., Tiaglik, A., Vuuregge,
539 A.H., Willems, R.A.L., Witkamp, D., et al. (2019). Co-administration of anti microRNA-124 and -137
540 oligonucleotides prevents hippocampal neural stem cell loss upon non-convulsive seizures. Front. Mol.

Neurosci. *12*.

Bonaguidi, M.A., Wheeler, M.A., Shapiro, J.S., Stadel, R.P., Sun, G.J., Ming, G.-L., and Song, H. (2011). In Vivo Clonal Analysis Reveals Self-Renewing and Multipotent Adult Neural Stem Cell Characteristics. Cell *145*, 1142–1155.

Braun, S.M.G., Machado, R.A.C., and Jessberger, S. (2013). Temporal Control of Retroviral Transgene Expression in Newborn Cells in the Adult Brain. Stem Cell Reports *1*, 114–122.

Castañeda, J., Genzor, P., Heijden, G.W., Sarkeshik, A., Yates, J.R., Ingolia, N.T., and Bortvin, A. (2014). Reduced pachytene pi <scp>RNA</scp> s and translation underlie spermiogenic arrest in <scp>M</scp> aelstrom mutant mice. EMBO J. *33*, 1999–2019.

Clarke, L.E., Liddelow, S.A., Chakraborty, C., Münch, A.E., Heiman, M., and Barres, B.A. (2018). Normal aging induces A1-like astrocyte reactivity. Proc. Natl. Acad. Sci. *115*, E1896–E1905.

Coufal, N.G., Garcia-Perez, J.L., Peng, G.E., Yeo, G.W., Mu, Y., Lovci, M.T., Morell, M., O'Shea, K.S., Moran, J. V., and Gage, F.H. (2009). L1 retrotransposition in human neural progenitor cells. Nature *460*, 1127–1131.

Czech, B., Munafò, M., Ciabrelli, F., Eastwood, E.L., Fabry, M.H., Kneuss, E., and Hannon, G.J. (2018). piRNA-Guided Genome Defense: From Biogenesis to Silencing. Annu. Rev. Genet. *52*, 131–157.

Dai, P., Wang, X., Gou, L.T., Li, Z.T., Wen, Z., Chen, Z.G., Hua, M.M., Zhong, A., Wang, L., Su, H., et al. (2019). A Translation-Activating Function of MIWI/piRNA during Mouse Spermiogenesis. Cell *179*, 1566-1581.e16.

Diaspro, A., and Bianchini, P. (2020). Optical nanoscopy. Riv. Del Nuovo Cim. 1–71.

Doetsch, F., Caille, I., Lim, D.A., Garcia-Verdugo, J.M., and Alvarez-Buylla, A. (1999). Subventricular zone astrocytes are neural stem cells in the adult mammalian brain. Cell *97*, 703–716.

Encinas, J.M., Michurina, T. V., Peunova, N., Park, J.H., Tordo, J., Peterson, D.A., Fishell, G., Koulakov, A., and Enikolopov, G. (2011). Division-coupled astrocytic differentiation and age-related depletion of neural stem cells in the adult hippocampus. Cell Stem Cell *8*, 566–579.

Escartin, C., Galea, E., Lakatos, A., O'Callaghan, J.P., Petzold, G.C., Serrano-Pozo, A., Steinhäuser, C., Volterra, A., Carmignoto, G., Agarwal, A., et al. (2021). Reactive astrocyte nomenclature, definitions, and future directions. Nat. Neurosci. *24*, 312–325.

569 Gainetdinov, I., Colpan, C., Arif, A., Cecchini, K., and Zamore, P.D. (2018). A Single Mechanism of
570 Biogenesis, Initiated and Directed by PIWI Proteins, Explains piRNA Production in Most Animals. Mol.
571 Cell *71*, 775-790.e5.
572 Ghosheh, Y., Seridi, L., Ryu, T., Takahashi, H., and Orlando, V. (2016). Characterization of piRNAs across
573 postnatal development in mouse brain. Nat. Publ. Gr. 1–7.
574 Girard, A., Sachidanandam, R., Hannon, G.J., and Carmell, M.A. (2006). A germline-specific class of small
575 RNAs binds mammalian Piwi proteins. Nature *442*, 199–202.
576 Huang, D.W., Sherman, B.T., and Lempicki, R.A. (2009). Systematic and integrative analysis of large gene
577 lists using DAVID bioinformatics resources. Nat. Protoc. *4*, 44–57.
578 Huang, H., Yu, X., Han, X., Hao, J., Zhao, J., Bebek, G., Bao, S., Prayson, R.A., Khalil, A.M., Jankowsky,
579 E., et al. (2021). Piwil1 Regulates Glioma Stem Cell Maintenance and Glioblastoma Progression. Cell Rep.
580 *34*, 108522.
581 Jain, G., Stuendl, A., Rao, P., Berulava, T., Pena Centeno, T., Kaurani, L., Burkhardt, S., Delalle, I.,
582 Kornhuber, J., Hüll, M., et al. (2019). A combined miRNA–piRNA signature to detect Alzheimer's disease.
583 Transl. Psychiatry *9*, 250.
584 Karolchik, D. (2004). The UCSC Table Browser data retrieval tool. Nucleic Acids Res. *32*, 493D – 496.
585 Keam, S.P., Young, P.E., McCorkindale, A.L., Dang, T.H.Y., Clancy, J.L., Humphreys, D.T., Preiss, T.,
586 Hutvagner, G., Martin, D.I.K., Cropley, J.E., et al. (2014). The human Piwi protein Hiwi2 associates with
587 tRNA-derived piRNAs in somatic cells. Nucleic Acids Res. *42*, 8984–8995.
588 Kirino, Y., and Mourelatos, Z. (2007). Mouse Piwi-interacting RNAs are 2′-O-methylated at their 3′ termini.
589 Nat. Struct. Mol. Biol. *14*, 347–348.
590 Kozomara, A., and Griffiths-Jones, S. (2014). MiRBase: Annotating high confidence microRNAs using deep
591 sequencing data. Nucleic Acids Res. *42*.
592 Krishan, (1975). Rapid flow cytofluorometric analysis of mammalian cell cycle by propidium iodide
593 staining. J. Cell Biol. 66, 188–193.
594 Langmead, B., and Salzberg, S.L. (2012). Fast gapped-read alignment with Bowtie 2. Nat. Methods *9*, 357–
595 359.
596 Lee, E.J., Banerjee, S., Zhou, H., Jammalamadaka, A., Arcila, M., Manjunath, B.S., and Kosik, K.S. (2011).

Identification of piRNAs in the central nervous system. Rna *17*, 1090–1099.

Leighton, L.J., Wei, W., Marshall, P.R., Ratnu, V.S., Li, X., Zajaczkowski, E.L., Spadaro, P.A., Khandelwal, N., Kumar, A., and Bredy, T.W. (2019). Disrupting the hippocampal Piwi pathway enhances contextual fear memory in mice. Neurobiol. Learn. Mem. *161*, 202–209.

Liddelow, S.A., Guttenplan, K.A., Clarke, L.E., Bennett, F.C., Bohlen, C.J., Schirmer, L., Bennett, M.L., Münch, A.E., Chung, W.-S., Peterson, T.C., et al. (2017). Neurotoxic reactive astrocytes are induced by activated microglia. Nature *541*, 481–487.

Liu, G.Y., and Sabatini, D.M. (2020). mTOR at the nexus of nutrition, growth, ageing and disease. Nat. Rev. Mol. Cell Biol. *21*, 183–203.

Love, M.I., Huber, W., and Anders, S. (2014). Moderated estimation of fold change and dispersion for RNA-seq data with DESeq2. Genome Biol. *15*.

Madisen, L., Zwingman, T.A., Sunkin, S.M., Oh, S.W., Zariwala, H.A., Gu, H., Ng, L.L., Palmiter, R.D., Hawrylycz, M.J., Jones, A.R., et al. (2010). A robust and high-throughput Cre reporting and characterization system for the whole mouse brain. Nat. Neurosci. *13*, 133–140.

Martín-Suárez, S., Valero, J., Muro-García, T., and Encinas, J.M. (2019). Phenotypical and functional heterogeneity of neural stem cells in the aged hippocampus. Aging Cell *18*, e12958.

Mignone, J.L., Kukekov, V., Chiang, A.S., Steindler, D., and Enikolopov, G. (2004). Neural Stem and Progenitor Cells in Nestin-GFP Transgenic Mice. J. Comp. Neurol. *469*, 311–324.

Mills, E.W., and Green, R. (2017). Ribosomopathies: There's strength in numbers. Science *358*, 1-8.

Muotri, A.R., Chu, V.T., Marchetto, M.C.N., Deng, W., Moran, J. V., and Gage, F.H. (2005). Somatic mosaicism in neuronal precursor cells mediated by L1 retrotransposition. Nature *435*, 903–910.

Nandi, S., Chandramohan, D., Fioriti, L., Melnick, A.M., Hébert, J.M., Mason, C.E., Rajasethupathy, P., and Kandel, E.R. (2016). Roles for small noncoding RNAs in silencing of retrotransposons in the mammalian brain. Proc. Natl. Acad. Sci. U. S. A. *113*, 12697–12707.

Nolde, M.J., Cheng, E. chun, Guo, S., and Lin, H. (2013). Piwi Genes Are Dispensable for Normal Hematopoiesis in Mice. PLoS One *8*, 1–8.

Ozata, D.M., Gainetdinov, I., Zoch, A., O'Carroll, D., and Zamore, P.D. (2019). PIWI-interacting RNAs: small RNAs with big functions. Nat. Rev. Genet. *20*, 89–108.

625 Patro, R., Duggal, G., Love, M.I., Irizarry, R.A., and Kingsford, C. (2017). Salmon provides fast and bias-
626 aware quantification of transcript expression. Nat. Methods *14*, 417–419.
627 Petrov, A.I., Kay, S.J.E., Gibson, R., Kulesha, E., Staines, D., Bruford, E.A., Wright, M.W., Burge, S., Finn,
628 R.D., Kersey, P.J., et al. (2015). RNAcentral: An international database of ncRNA sequences. Nucleic Acids
629 Res. 43, D123–D129.
630 Paxinos, G. and F.K.B.J. (2001). The Mouse Brain in Stereotaxic Coordinates. 2nd Edition.
631 Perera, B.P.U., Tsai, Z.T.Y., Colwell, M.L., Jones, T.R., Goodrich, J.M., Wang, K., Sartor, M.A., Faulk, C.,
632 and Dolinoy, D.C. (2019). Somatic expression of piRNA and associated machinery in the mouse identifies
633 short, tissue-specific piRNA. Epigenetics *14*, 504–521.
634 Pons-Espinal, M., de Luca, E., Marzi, M.J., Beckervordersandforth, R., Armirotti, A., Nicassio, F., Fabel, K.,
635 Kempermann, G., and De Pietri Tonelli, D. (2017). Synergic Functions of miRNAs Determine Neuronal Fate
636 of Adult Neural Stem Cells. Stem Cell Reports *8*, 1046–1061.
637 Pons-Espinal, M., Gasperini, C., Marzi, M.J., Braccia, C., Armirotti, A., Pötzsch, A., Walker, T.L., Fabel,
638 K., Nicassio, F., Kempermann, G., et al. (2019). MiR-135a-5p Is Critical for Exercise-Induced Adult
639 Neurogenesis. Stem Cell Reports *12*, 1298–1312.
640 Quinlan, A.R., and Hall, I.M. (2010). BEDTools: A flexible suite of utilities for comparing genomic features.
641 Bioinformatics *26*, 841–842.
642 De Rie, D., Abugessaisa, I., Alam, T., Arner, E., Arner, P., Ashoor, H., Åström, G., Babina, M., Bertin, N.,
643 Burroughs, A.M., et al. (2017). An integrated expression atlas of miRNAs and their promoters in human and
644 mouse. Nat. Biotechnol. *35*, 872–878.
645 Robinson, M.D., and Oshlack, A. (2010). A scaling normalization method for differential expression analysis
646 of RNA-seq data. Genome Biol. *11*, R25.
647 Rojas-Ríos, P., and Simonelig, M. (2018). piRNAs and PIWI proteins: regulators of gene expression in
648 development and stem cells. Development *145*, dev161786.
649 Schindelin, J., Arganda-Carreras, I., Frise, E., Kaynig, V., Longair, M., Pietzsch, T., Preibisch, S., Rueden,
650 C., Saalfeld, S., Schmid, B., et al. (2012). Fiji: an open-source platform for biological-image analysis. Nat.
651 Methods *9*, 676–682.
652 Schouten, M., Bielefeld, P., Garcia-Corzo, L., Passchier, E.M.J., Gradari, S., Jungenitz, T., Pons-Espinal, M.,

653 Gebara, E., Martín-Suárez, S., Lucassen, P.J., et al. (2020). Circadian glucocorticoid oscillations preserve a
654 population of adult hippocampal neural stem cells in the aging brain. Mol. Psychiatry *25*, 1382–1405.
655 Sharma, A.K., Nelson, M.C., Brandt, J.E., Wessman, M., Mahmud, N., Weller, K.P., and Hoffman, R.
656 (2001). Human CD34(+) stem cells express the hiwi gene, a human homologue of the Drosophila gene piwi.
657 Blood *97*, 426–434.
658 Sierra, A., Martín-Suárez, S., Valcárcel-Martín, R., Pascual-Brazo, J., Aelvoet, S.-A., Abiega, O., Deudero,
659 J.J., Brewster, A.L., Bernales, I., Anderson, A.E., et al. (2015). Neuronal Hyperactivity Accelerates
660 Depletion of Neural Stem Cells and Impairs Hippocampal Neurogenesis. Cell Stem Cell *16*, 488–503.
661 Toda, T., Parylak, S.L., Linker, S.B., and Gage, F.H. (2019). The role of adult hippocampal neurogenesis in
662 brain health and disease. Mol. Psychiatry *24*, 67–87.
663 Torres, A.G., Reina, O., Attolini, C.S.O., and Ribas De Pouplana, L. (2019). Differential expression of
664 human tRNA genes drives the abundance of tRNA-derived fragments. Proc. Natl. Acad. Sci. U. S. A. *116*,
665 8451–8456.
666 Vicidomini, G., Bianchini, P., and Diaspro, A. (2018). STED super-resolved microscopy. Nat. Methods *15*,
667 173–182.
668 Viero, G., Lunelli, L., Passerini, A., Bianchini, P., Gilbert, R.J., Bernabò, P., Tebaldi, T., Diaspro, A.,
669 Pederzolli, C., and Quattrone, A. (2015). Three distinct ribosome assemblies modulated by translation are the
670 building blocks of polysomes. J. Cell Biol. *208*, 581–596.
671 Wakisaka, K.T. (2019). The dawn of pirna research in various neuronal disorders. Front. Biosci. *24*, 1440–
672 1451.
673 Walker, T.L., and Kempermann, G. (2014). One mouse, two cultures: Isolation and culture of adult neural
674 stem cells from the two neurogenic zones of individual mice. J. Vis. Exp. 1-9.
675 Walker, T.L., Overall, R.W., Vogler, S., Sykes, A.M., Ruhwald, S., Lasse, D., Ichwan, M., Fabel, K., and
676 Kempermann, G. (2016). Lysophosphatidic Acid Receptor Is a Functional Marker of Adult Hippocampal
677 Precursor Cells. Stem Cell Reports *6*, 552–565.
678 Waterston, R.H., Lindblad-Toh, K., Birney, E., Rogers, J., Abril, J.F., Agarwal, P., Agarwala, R., Ainscough,
679 R., Alexandersson, M., An, P., et al. (2002). Initial sequencing and comparative analysis of the mouse
680 genome. Nature *420*, 520–562.

Yu, C..-W. (1992). The assessment of cellular proliferation by immunohistochemistry: a review of currently available methods and their applications.

Zhang, P., Si, X., Skogerbï¿½, G., Wang, J., Cui, D., Li, Y., Sun, X., Liu, L., Sun, B., Chen, R., et al. (2014). PiRBase: A Web resource assisting piRNA functional study. Database *2014*, 1–7.

Zhao, P., Yao, M., Chang, S., Gou, L., Liu, M., and Qiu, Z. (2015). Novel function of PIWIL1 in neuronal polarization and migration via regulation of microtubule-associated proteins. Mol. Brain 1–12.

**Acknowledgments**

We are grateful to G. Hannon (Cambridge, UK) for providing Mili, Miwi antibodies; G. Enikolopov (Stony Brook Univ. NY, USA) for the Nestin-GFP mouse. We thank IIT technical staff (S. Bianchi; M. Pesce; E. Albanesi, M. Morini, D. Vozzi) for excellent assistance and L. Pandolfini (IIT-CHT Genoa, Italy) for advice in piRNA resistance to periodate oxidation and alkaline ß-elimination protocol. **Funding:** This study was supported by Fondazione Istituto Italiano di Tecnologia; by Fondazione Cariplo Grant #2015-0590 and AIRC-IG 2017 # 20106 to DDPT. P.B. (UvA) and C.P.F. were funded by an ERA-NET-NEURON EJTC 2016 grant and by The Netherlands Organization for Scientific research (NWO). We apologize to those colleagues whose work could not be cited due to space limitations.

**Author contributions**

Conceptualization: C.G., D.D.P.T; Methodology and experiments: C.G, K.T., R.P., D.M., P.B. (UVA), C.P.F., P.B. (IIT), M.S., M.P.E.; *In silico* analysis: A.L.V, R.M.C., G.P., K.T.; Data Curation and visualization: C.G.; Writing – original draft preparation: C.G., D.D.P.T; –Editing: all the authors; Supervision: R.S., A.D., C.P.F., P.C., S.G.; D.D.P.T.; Project administration: D.D.P.T.; Funding acquisition: D.D.P.T.

**Declaration of interests**

The authors declare no competing interests.

708 **Figure legends**

709 **Fig. 1. Hippocampal expression of Mili is enriched in aNPCs and decreases during neurogenesis.**

710 (A) Levels of PIWIL1 (Miwi), PIWIL2 (Mili) and PIWIL3 (Miwi2) transcripts in RNA seq. data from aNPCs
711 cultures in proliferative (Days of differentiation –DIF– 0) and differentiation media (DIF 4 to 14). (B) Mili
712 protein abundance in undifferentiated aNPCs (DIF0) and upon viral-induced neurogenesis (DIF4-14). (C)
713 Miwi and (D) Mili protein abundance in extracts from postnatal mouse testis, hippocampus and from
714 undifferentiated aNPCs cultures. (E) Mili protein abundance in in extracts from cultured mouse hippocampal
715 neurons and undifferentiated aNPCs. (F) Mili (white) expression in Td+ NSC (red) in hippocampal subgranular
716 zone (SGZ); arrows indicate Td+ Mili + double-positive cells. (G) Scheme of the experiment (top), *Mili* mRNA
717 expression in sorted Td+ and Td– cells after *in vivo* transduction with split-Cre viruses in the hippocampus
718 (bottom). Data are expressed as mean ± SEM, n = 3 independent experiments. t-Student test or one-way
719 ANOVA Bonferroni as post hoc: *$p < 0.05$, **$p < 0.01$, **** $p < 0.0001$. GCL, granular cell layer; H, Hilus.
720 Scale bars: 10 µm.

721

722 **Fig. 2. Level of piRNAs parallels Mili abundance in neurogenesis.**

723 (A) Size distribution of piRNA reads. (B) Uridine bias at piRNA 5' ends. (C) Probability of distances from
724 the 5'ends of putative secondary piRNAs to the 5'ends of putative primary piRNAs. Note that 5' termini of
725 putative primary and secondary piRNAs derived from the same cluster tend to concatenate around the '0'
726 mark, as reported in other animals. Distance probability was assayed for unique piRNAs (length between 15-
727 35 nucleotides), without taking into account abundance, by locally weighted smoothing linear regression
728 (LOWESS). (D) RNA relative expression of four of the top abundant piRNAs (in H) and two control
729 snoRNAs (202 and 135) in aNPC, upon treatment with sodium periodate ($NaIO_4$) or water and alkaline ß-
730 elimination. Synthetic RNA oligos were used as negative (Unmethylated, UnMet) and positive (2'-O-
731 methylated, 2'OMet) controls, respectively. Note that presence of 3'-end 2'-O-methylation in positive
732 control and piRNAs confers them resistance to periodate oxidation and alkaline ß-elimination, in contrast to
733 their depletion in UnMet negative control and snoRNAs. (E) *Mili* mRNA (left) and protein (right) levels in
734 aNPCs upon viral transduction of scrambled shRNA (Control) or shRNA targeting *Mili* (Mili KD). (F)
735 Expression of four of the most abundant piRNA clusters in control and Mili KD aNPCs. (G) Genomic

location of 298 piRNA clusters on mm9. (H) Mean reads of piRNA clusters in aNPCs (DIF0) and upon viral-induced neurogenesis (DIF4-7), where the total number of filtered reads in each library ranges between 1,4 - 4,4 x $10^6$. (I) (left) Schematic representation of the experiment; (right) expression of four of the most abundant piRNA clusters in sorted Td+ and Td- cells 10 dpi of split-Cre viruses in hippocampus. (L) Expression of piRNA clusters (left) and piR-cluster 1 (right) in human NSC and astrocytes. Data are expressed as mean ± SEM, n = 2 (A-C, G-H) and n = 3 (D-F, I) independent experiments. t-Student test as post hoc: *p < 0.05, **p < 0.01, *** p < 0.001, **** p < 0.0001.

**Fig. 3. The piRNA pathway sustains proper neurogenesis.**

(A) Scheme of the *in vivo* experiment. (B) *Mili* mRNA (left), protein (middle) and *Gfap* mRNA (right) levels in the hippocampus 48 hours after the injection of scrambled (Control) or GapmeR against Mili (Mili KD). (C) Light-microscopy images of postnatal hippocampal sections, immunostained for GFAP, 30 dpi of scrambled (Control, left hemisphere) and GapmeR against Mili (Mili KD, right hemisphere). (D) (Left) Immunostaining for GFAP (green), BrdU (red), NeuN (white) and nuclear DNA (blue) in the hippocampus 30 dpi of scrambled (Control) or GapmeR against Mili (Mili KD); (right) percentages of NeuN+BrdU+ (white arrowheads), or GFAP+BrdU+ (yellow arrowheads) over total BrdU+ cells. (E) mRNA expression of reactive astrocyte markers in the hippocampus 48h upon injection of scrambled (control) or GapmeR against Mili (Mili KD). (F) *Mili* mRNA (left) and piR-cluster 1 (right) expression in sorted GFP+ NSCs from Nestin-GFP mice treated with Saline (Control) or Kainic Acid (KA). Data are expressed as mean ± SEM, n = 3 independent experiments (A-C); n=5 (E); n = 7 (F, G); n = 3 (H, I). t-Student test as post hoc: *p < 0.05, **p < 0.01, **** p < 0.0001. Scale bars: 1 mm (C); 100 µm (D).

**Fig. 4. Inhibition of the piRNA pathway in aNPCs induces senescence-associated phenotypes**

(A) Heatmap showing the mRNA expression of genes involved in immune-modulatory and senescence associated genes in differentiating aNPCs at DIF4 upon Mili KD compared to control cells. Expression level represented in Transcript per Million (TPM). (B) Bright field microscopy images (left) and quantification (right) of ß-galactosidase positive cells as percent of total cells upon Mili KD or control, 48 h after induction of spontaneous differentiation. (C) Fluorescence microscopy images (left) and quantification (right) of control

764 or Mili KD aNPCs 48h after spontaneous differentiation, immunostained with anti-BrdU (white) and Ki67
765 (purple) antibodies. (Right) Percentage of BrdU+ and Ki67- cells over BrdU+ cells. (D) (Top) Representative
766 cell cycle analysis of propidium iodide staining by flow cytometry; (Bottom) Percentage of aNPCs in G0/G1,
767 S and G2/M phases 48h after spontaneous differentiation. (E, F) Relative abundance of cell cycle-dependent
768 genes (E) and involved in cell cycle (F) in Control and Mili KD aNPCs 48 hours (E) or DIF4 (F) after
769 spontaneous differentiation. (G) (left) Scheme of the *in vivo* experiment; (right) *Mili* mRNA expression in
770 Nestin+ sorted cells from young (6 weeks) and old (56 weeks) mice. Data are expressed as mean ± SEM, n =
771 3 independent, (in A, 2 separate flow cells per sample). t-Student test as post hoc: $*p < 0.05$, $**p < 0.01$,
772 $***p < 0.001$, **** $p < 0.0001$. Scale bar, 50 µm.
773

774 **Fig 5. piRNAs target noncoding RNAs and mRNAs involved in ribosome assembly and translation.**
775 (A, B) Pie plots showing proportions of noncoding RNAs predicted targets of piRNAs in undifferentiated
776 aNPCs (A, DIF0) and upon induction of neurogenesis (B, DIF4-7). (C) Transcription levels of SINE B1 and
777 5S rRNA, and (D) transcription levels of LINE1 5'UTR in the Mili KD aNSCs (DIF0) and differentiating
778 aNPC (DIF4-7). (E) Total counts of upregulated (black bars) and downregulated genes (white bars), for all
779 genes, all piRNA targeted genes and those with piRNA homology (indicated). (F) Scatter plot of all detected
780 genes in control or Mili KD aNPCs (black circles), piRNA target (red circles) and those with piRNA homology
781 (blue dots). (G) The log2 fold-change of significantly altered genic mRNA transcripts (abscissa) plotted with
782 the raw number of unique piRNA sequences qualified as targeting molecules (ordinate) for all modulated genes
783 (black circles), and piRNA-targeted genes (red dots), identified by RNA-Seq. The modulated genes without
784 targeting piRNAs concatenate at the bottom at the 'y = 0' value. Total rage, inset. (H) The log2 fold-change
785 of significantly altered piRNA-targeted gene mRNA transcripts (abscissa) plotted with the summed levels of
786 all mRNA-targeting (complementary) piRNA molecules (ordinate), identified by RNA-Seq. (I) Bar graph
787 showing the top biological pathways significantly upregulated upon Mili KD; Numbers in each category
788 indicate gene counts. Data are expressed as mean ± SEM, n = 3 independent experiments. t-Student test as
789 post hoc: $*p < 0.05$, $**p < 0.01$ (C &D). Significant difference was detected by the one-way ANOVA, $p<0.05$
790 (G & H). Data are expressed in transcripts per million (TPM) as the mean levels of 6 sequencing runs for 3

791 samples. (E-I) transcriptome profiling at DIF4. Outliers (mean calculation) were detected by more than three
792 mean absolute deviations, for a final 'n' value between 4 and 6 samples.
793
794 **Fig. 6. Inhibition of the piRNA pathway in aNPCs enhances polysome assembly and results in higher**
795 **protein synthesis upon differentiation.**
796 (A, B) Microscopy images (Middle cut: g-STED nanoscopy; Bottom: Confocal; Top: analysis) of control and
797 Mili KD aNPCs (DIF 0 and 7) immunostained for the ribosomal protein RPL26. (Right) normalized
798 distributions of the occupancy, concentration and average of particle size of each polyribosome particle in the
799 indicated cells. (C) Protein synthesis rate (right) as determined by OPP incorporation assay with flow
800 cytometry (left) in control and Mili KD undifferentiated (DIF0) and differentiating (DIF 7) aNPCs. Scale bars:
801 2 (A); 10 (B) μm. Data are expressed as mean ± SEM, n = 3 independent experiments. t-Student test as post
802 hoc: $*p < 0.05$.

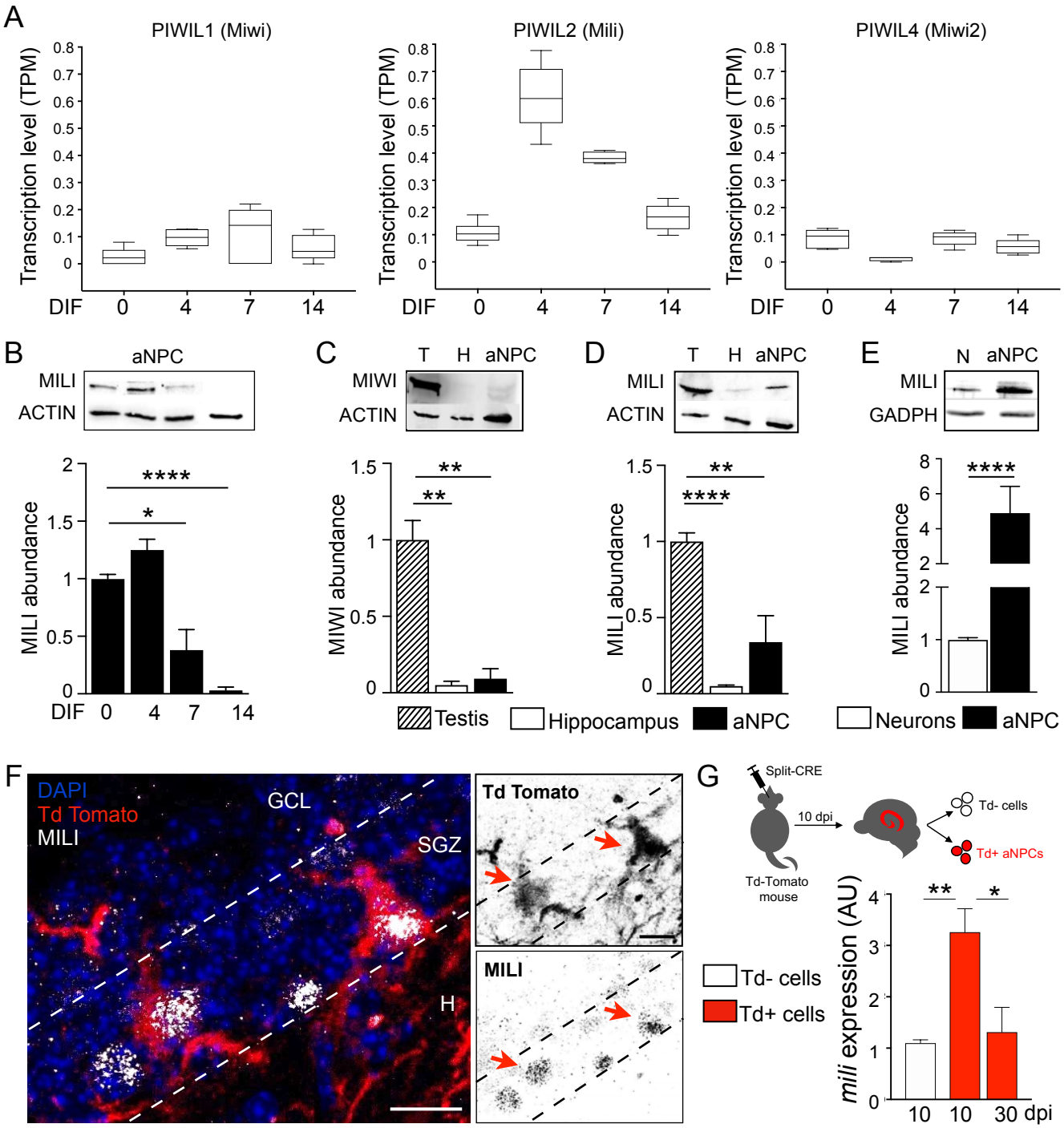
A
PIWIL1 (Miwi)
PIWIL2 (Mili)
PIWIL4 (Miwi2)
Transcription level (TPM)
DIF 0 4 7 14
B
aNPC
MILI
ACTIN
MILI abundance
C
T H aNPC
MIWI
ACTIN
MIWI abundance
D
T H aNPC
MILI
ACTIN
MILI abundance
E
N aNPC
MILI
GADPH
MILI abundance
Testis
Hippocampus
aNPC
Neurons
aNPC
F
DAPI
Td Tomato
MILI
GCL
SGZ
H
Td Tomato
MILI
G
Split-CRE
10 dpi
Td-Tomato mouse
Td- cells
Td+ aNPCs
Td- cells
Td+ cells
mili expression (AU)
10 10 30 dpi

**Fig. 1**

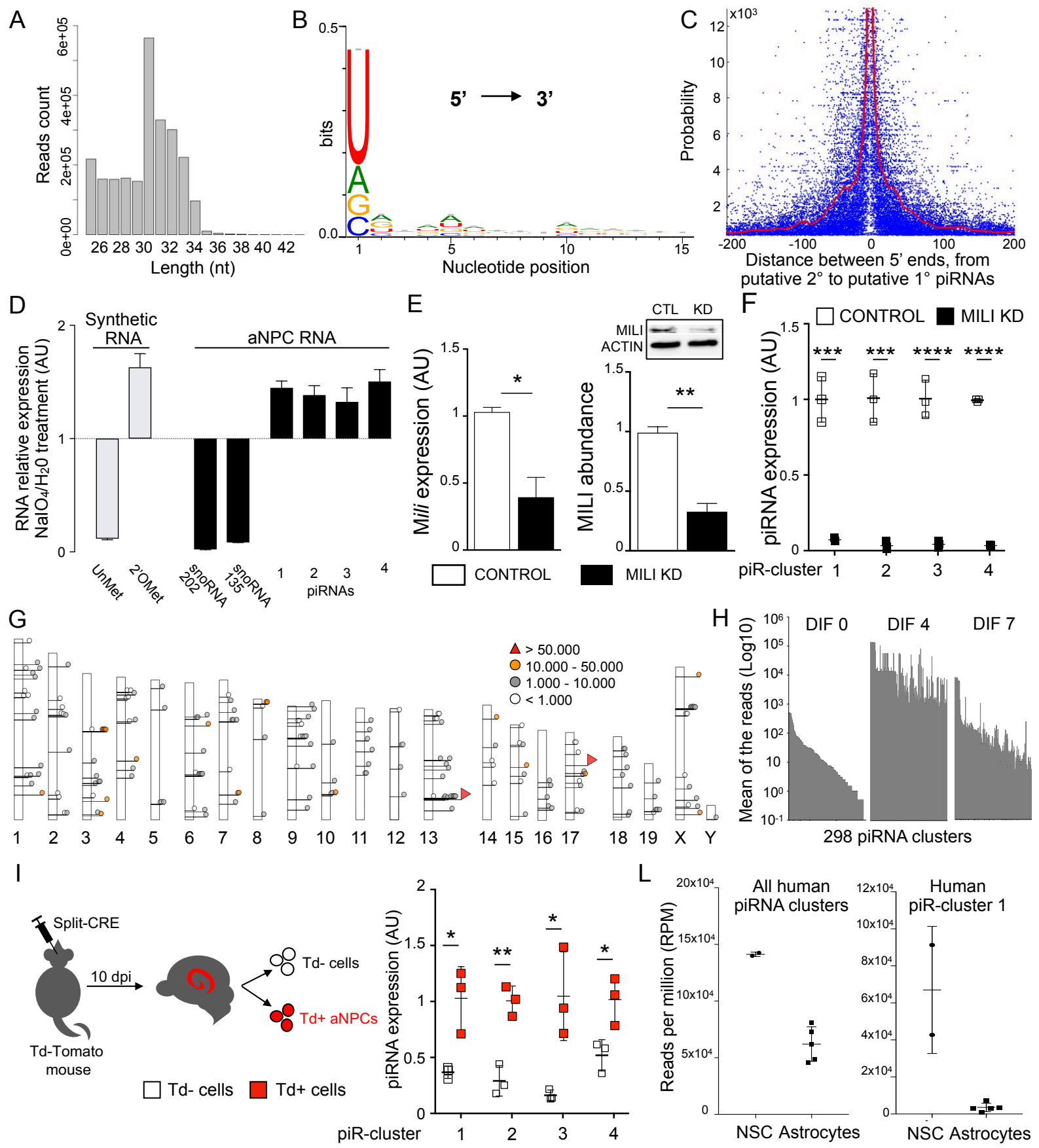
A
Reads count
Length (nt)
B
bits
5' → 3'
Nucleotide position
C
Probability
Distance between 5' ends, from putative 2° to putative 1° piRNAs
D
Synthetic RNA
aNPC RNA
RNA relative expression NaIO4/H20 treatment (AU)
UnMet
2'OMet
snoRNA 202
snoRNA 135
piRNAs
E
Mili expression (AU)
CTL
KD
MILI
ACTIN
MILI abundance
CONTROL
MILI KD
F
CONTROL
MILI KD
piRNA expression (AU)
piR-cluster
G
> 50.000
10.000 - 50.000
1.000 - 10.000
< 1.000
H
DIF 0
DIF 4
DIF 7
Mean of the reads (Log10)
298 piRNA clusters
I
Split-CRE
10 dpi
Td-Tomato mouse
Td- cells
Td+ aNPCs
Td- cells
Td+ cells
piRNA expression (AU)
piR-cluster
L
All human piRNA clusters
Human piR-cluster 1
Reads per million (RPM)
NSC
Astrocytes

**Fig. 2**

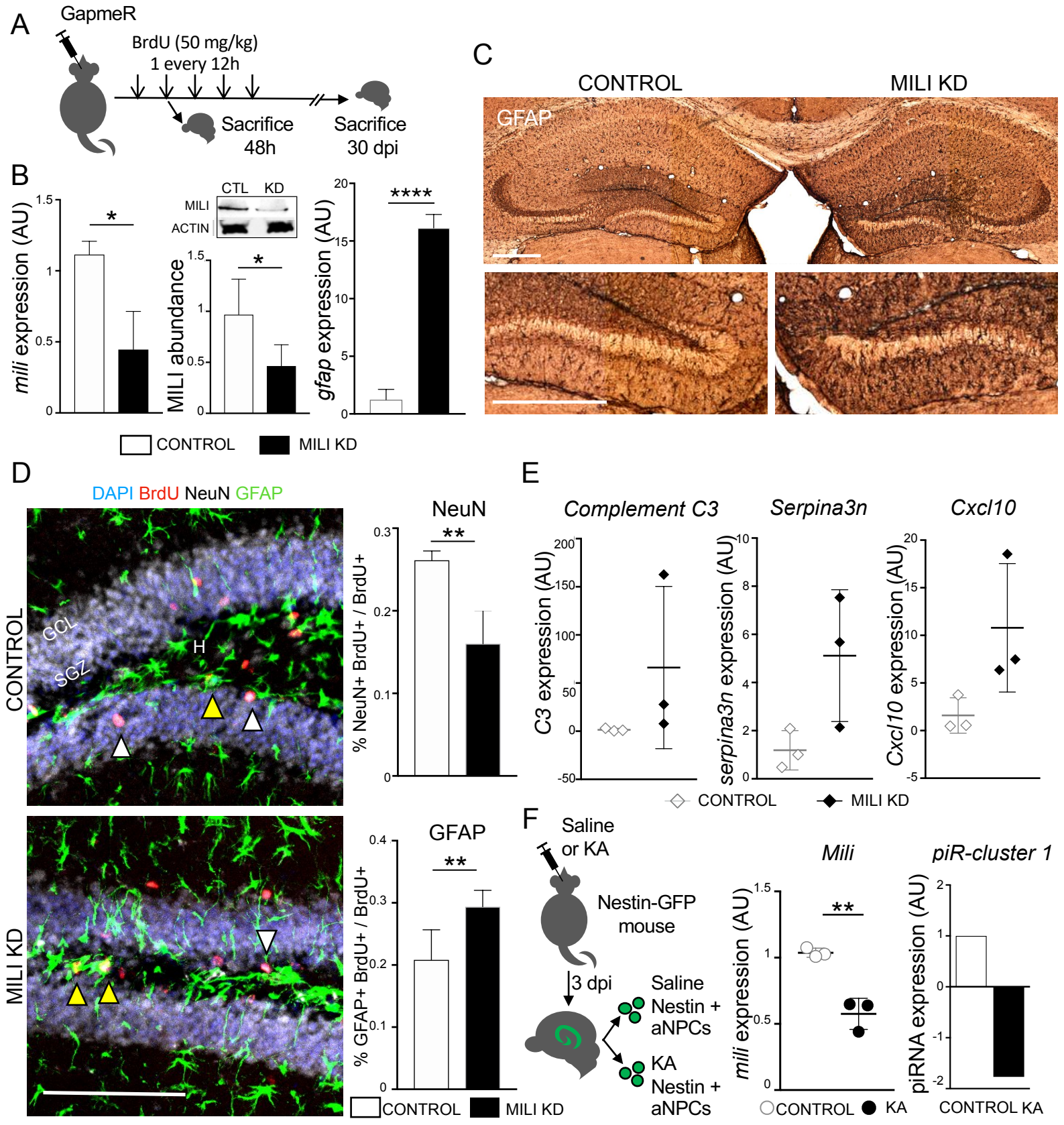
A
GapmeR
BrdU (50 mg/kg)
1 every 12h
Sacrifice
48h
Sacrifice
30 dpi
B
mili expression (AU)
CTL
KD
MILI
ACTIN
MILI abundance
gfap expression (AU)
CONTROL
MILI KD
C
CONTROL
MILI KD
GFAP
D
DAPI BrdU NeuN GFAP
CONTROL
MILI KD
GCL
SGZ
H
NeuN
% NeuN+ BrdU+ / BrdU+
GFAP
% GFAP+ BrdU+ / BrdU+
E
Complement C3
Serpina3n
Cxcl10
C3 expression (AU)
serpina3n expression (AU)
Cxcl10 expression (AU)
F
Saline
or KA
Nestin-GFP
mouse
3 dpi
Saline
Nestin +
aNPCs
KA
Nestin +
aNPCs
Mili
piR-cluster 1
mili expression (AU)
piRNA expression (AU)
KA
CONTROL KA

**Fig. 3**

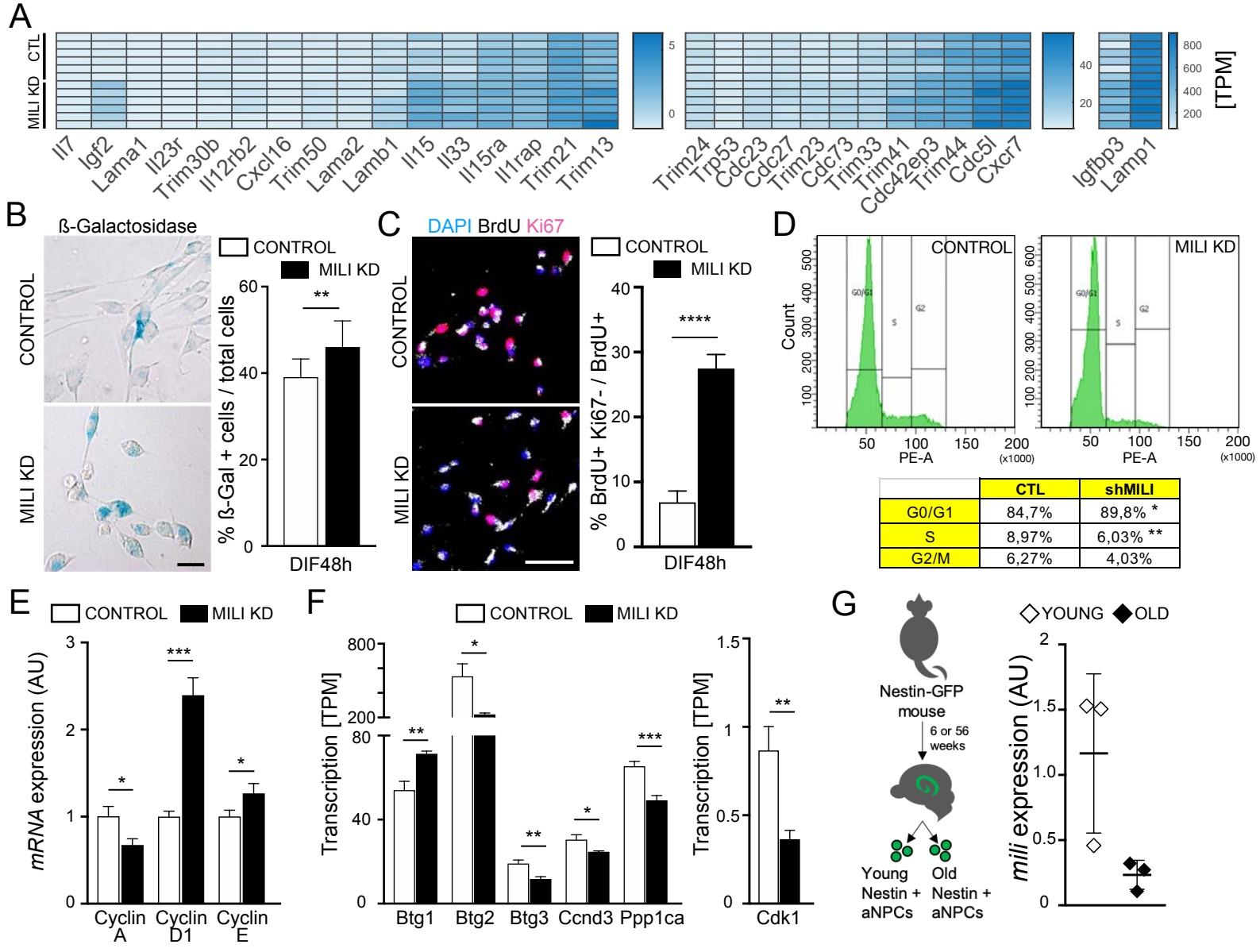


| | CTL | shMILI |
|---|---|---|
| G0/G1 | 84,7% | 89,8% * |
| S | 8,97% | 6,03% ** |
| G2/M | 6,27% | 4,03% |

**Fig. 4**

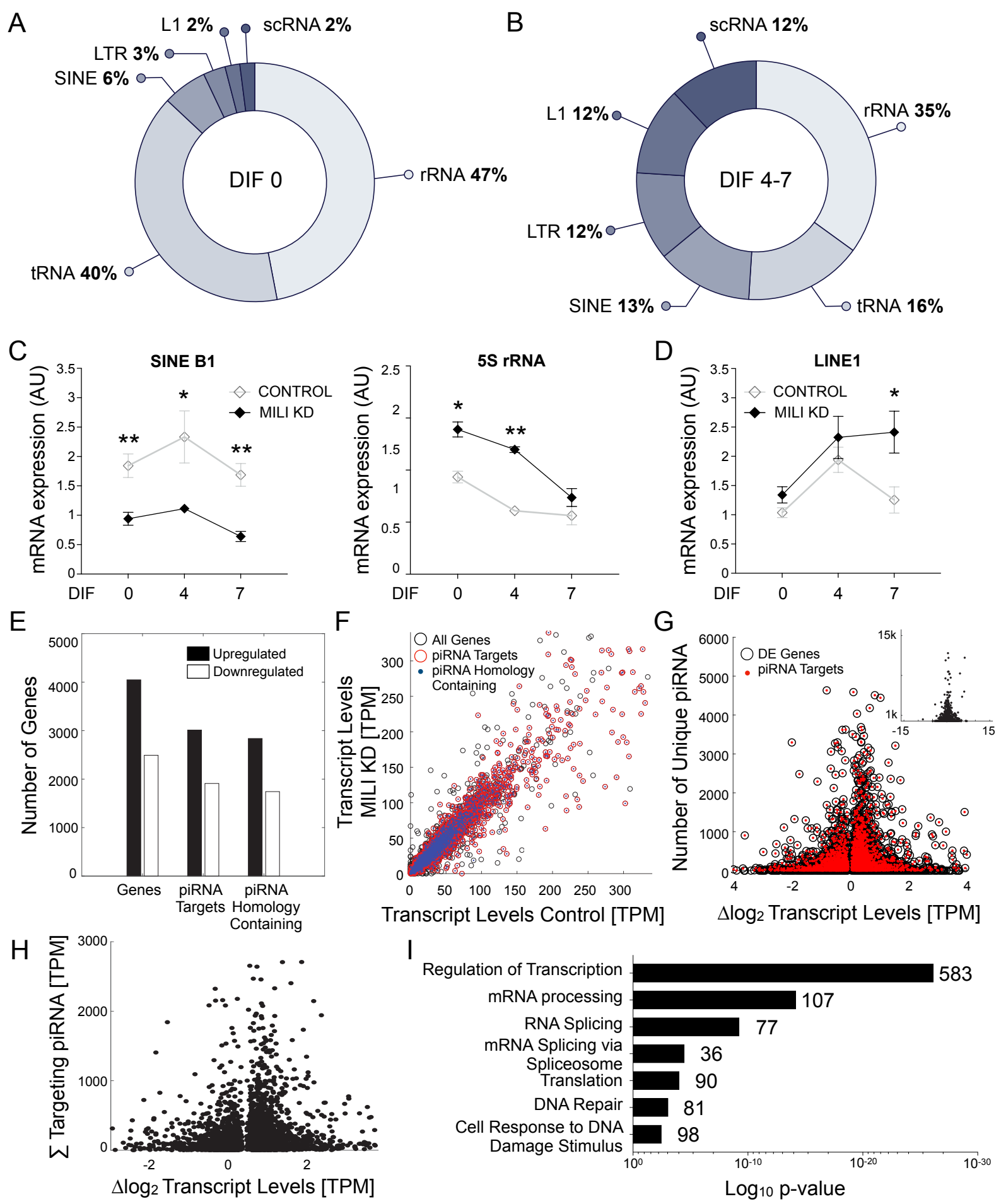
A
L1 2%
scRNA 2%
LTR 3%
SINE 6%
DIF 0
rRNA 47%
tRNA 40%
B
scRNA 12%
L1 12%
rRNA 35%
DIF 4-7
LTR 12%
SINE 13%
tRNA 16%
C
SINE B1
mRNA expression (AU)
CONTROL
MILI KD
DIF 0 4 7
5S rRNA
D
LINE1
E
Number of Genes
Upregulated
Downregulated
Genes
piRNA Targets
piRNA Homology Containing
F
All Genes
piRNA Targets
piRNA Homology Containing
Transcript Levels MILI KD [TPM]
Transcript Levels Control [TPM]
G
DE Genes
piRNA Targets
Number of Unique piRNA
Δlog2 Transcript Levels [TPM]
H
∑ Targeting piRNA [TPM]
Δlog2 Transcript Levels [TPM]
I
Regulation of Transcription 583
mRNA processing 107
RNA Splicing 77
mRNA Splicing via Spliceosome 36
Translation 90
DNA Repair 81
Cell Response to DNA Damage Stimulus 98
Log10 p-value

**Fig.5**

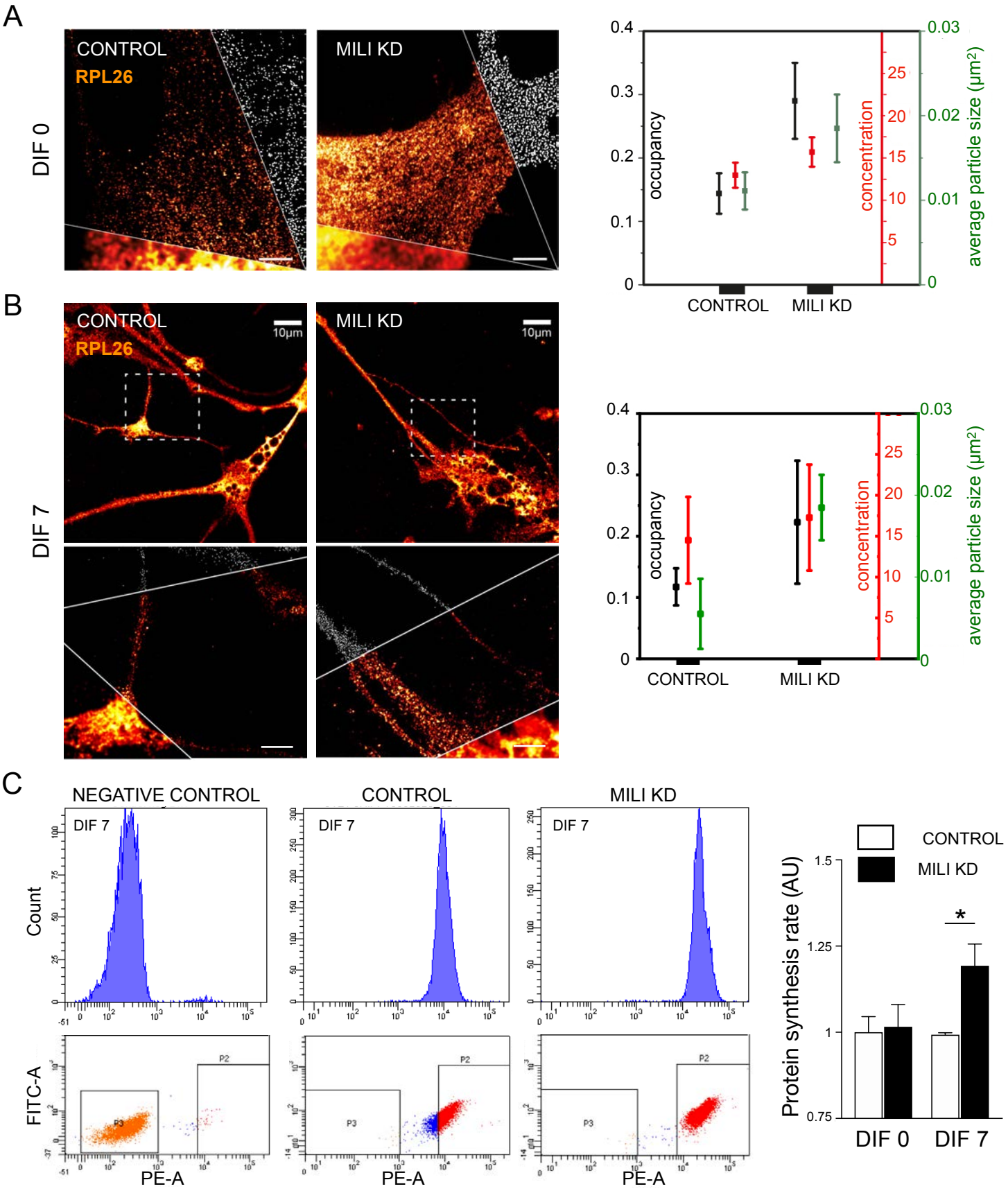
A
DIF 0
CONTROL
RPL26
MILI KD
occupancy
concentration
average particle size (µm²)
CONTROL
MILI KD
B
DIF 7
CONTROL
RPL26
MILI KD
10µm
10µm
occupancy
concentration
average particle size (µm²)
CONTROL
MILI KD
C
NEGATIVE CONTROL
CONTROL
MILI KD
DIF 7
Count
FITC-A
PE-A
P2
P3
CONTROL
MILI KD
Protein synthesis rate (AU)
DIF 0
DIF 7
*

**Fig. 6**